# Emission of unstable clusters from hot Yb compound nuclei

R. J. Charity and L. G. Sobotka
*Department of Chemistry, Washington University, St. Louis, Missouri 63130*

J. Cibor,* K. Hagel, M. Murray, J. B. Natowitz, and R. Wada
*Cyclotron Institute, Texas A&M University, College Station, Texas 77843*

Y. El Masri
*Institut de Physique Nucléaire, Université Catholique de Louvain, B-1348 Louvain-la-Neuve, Belgium*

D. Fabris, G. Nebbia, and G. Viesti
*INFN and Dipartimento di Fisica, Universitá di Padova, I-35131 Padova, Italy*

M. Cinausero, E. Fioretto, and G. Prete
*INFN Laboratori Nazionali di Legnaro, I-35020 Legnaro (Padova), Italy*

A. Wagner† and H. Xu
*National Superconducting Cyclotron Laboratory, Michigan State University, East Lansing, Michigan 48824*
(Received 13 June 2000; published 23 January 2001)

Neutrons and isotopically resolved light charged particles have been detected in coincidence with evaporation residues produced in the reaction $E/A=11$ MeV $^{60}$Ni+$^{100}$Mo. Multiplicities of evaporated particle-unstable clusters have been determined from correlations in the emission of these light particles. The decay of the short-lived $^{5}$He and $^{8}$Be ($E^{*}=3.04$ MeV) states was found to be affected by the Coulomb field of the compound nucleus in accordance with theoretical estimates. The contributions to the measured kinetic-energy distributions of stable fragments from the sequential decay of the unstable clusters was examined. Overall, the contributions from secondary fragments do not greatly influence the spectral shapes and specifically the location of the spectral peaks are not significantly shifted down in energy due to the presence of these secondary fragments. Therefore contrary to the suggestion of Charity *et al.* [Phys. Rev. C **56**, 873 (1997)], the lower peak energy of the experimental $\alpha$-particle spectrum as compared to standard statistical-model calculations cannot be attributed to sequential $\alpha$ particles from $^{5}$He and other clusters. Only for the extreme ''sub-barrier'' regions of the $\alpha$-particle, deuteron, $^{6,7}$Li, and $^{8}$Be spectra was the sequential contribution found to be dominant. Statistical-model calculations incorporating large initial deformations are shown to provide enhancements in the yield of low-energy fragments which are roughly appropriate for all the detected isotopes. This suggests that the origin of the sub-barrier enhancements may be a result of evaporation from highly deformed systems which are either produced dynamically during the fusion process or by thermal shape fluctuations.

DOI: 10.1103/PhysRevC.63.024611 PACS number(s): 25.70.Gh, 24.60.Dr, 25.70.Mn

## I. INTRODUCTION

Experimental studies of $\alpha$-particle evaporation from hot compound nuclei have found that the measured kinetic-energy spectrum is enhanced in the sub-barrier region compared to standard statistical-model calculations [1–10]. The peak in the experimental spectrum is typically shifted down in energy compared to these statistical-model predictions. Standard statistical-model calculations use ''spherical'' transmission coefficients obtained from the inverse absorption process of the $\alpha$ particle by a ground-state nucleus. The sub-barrier enhancement may thus indicate a different Coulomb barrier for the evaporation process compared to the barrier for this absorption process. A number of studies have been able to reproduce the measured $\alpha$-particle spectra by introducing into the statistical-model calculations a distribution of Coulomb barriers associated with a fixed deformation of the compound nucleus [1,3,4,8,10]. Emissions associated with the lower Coulomb barriers of this distribution populate the low-energy ''sub-barrier'' region which lies below the peak in the kinetic-energy spectrum. Recently, calculations considering not just a single deformation, but rather the thermal distribution of nuclear shapes, have also been able to reproduce experimental spectra for excitation energies of $\approx$100 MeV or less [11]. However, for high enough excitation energies, the shape distribution is not expected to be thermalized before evaporation commences and the $\alpha$-particle spectrum should reflect to some extent the deformation of the fusing system at the point when most of the excitation energy is dissipated.

Previously we had also suggested an alternative explanation of the sub-barrier enhancement at high excitation ener-

*Present address: H. Niewodniczański Institute of Nuclear Physics, Kraków, Poland.

†Present address: Forschungszentrum Rossendorf e.V., Dresden, Germany.

 

gies as potentially due to the emission of unstable clusters which sequentially decay producing $\alpha$ particles [9]. Statistical-model calculations incorporating the emission and decay of such clusters were found to account for a large fraction of the experimental ''sub-barrier'' enhancement in the $^{64}$Ni+$^{100}$Mo reactions. The largest contribution to the predicted sub-barrier enhancement is from $^{5}$He fragments which decay to $n-\alpha$ pairs. The Coulomb barrier for $^{5}$He emission is expected to be smaller than that for direct $\alpha$-particle emission as a $^{5}$He fragment is predicted to have a more diffuse surface [12]. Furthermore as the secondary $\alpha$ particles have approximately 80% of the initial $^{5}$He kinetic energy, the energy spectrum of these secondary particles extend down to lower kinetic energies compared to the directly emitted particles. By adjusting the $^{5}$He Coulomb barrier it was even possible to account for all of the experimental enhancement.

In order to determine the extent of the sub-barrier $\alpha$-particle enhancement from the emission of $^{5}$He and other unstable clusters, a study of the correlated emission of light particles (neutrons and charged particles) in coincidence with evaporation residues was undertaken. The reaction studied is $E/A=11$ MeV $^{60}$Ni+$^{100}$Mo, which is similar to the $E/A=9$ and 10 MeV $^{64}$Ni+$^{100}$Mo reactions of Ref. [9] for which statistical-model calculations reproduced the $\alpha$-particle spectrum when $\approx$30% of these particles are secondary. Thus if these calculations are correct, then the correlated emission of $\alpha$ particles and neutrons should be substantial and easily observable.

On the other hand, if deformation is the cause of the effect, then the spectra of all light charged particles should show consistent enhancements increasing with the $Z$ of the emitted fragment. Therefore kinetic-energy spectra were measured for isotopes with $Z=1-4$ and compared to statistical model predictions for spherical and deformed compound nuclei.

The chosen reaction is also identical to that studied by Gonin *et al.* [5,13], who reported substantially larger neutron and smaller charged-particle multiplicities compared to statistical-model predictions. These experimental multiplicities imply that the evaporation residues are significantly proton rich (past the present limits of known isotopes) compared to their predicted location near the evaporation attractor line [14]. If correct, it indicates that evaporation from hot compound nuclei could be a useful mechanism to create such proton-rich systems. The present study, although not optimized for this purpose, should allow these multiplicities to be verified if correct.

The details of the experimental apparatus are discussed in Sec. II while the analysis of the experimental results is described in Sec. III. The influence that secondary particles have on the shape of light-particle kinetic-energy spectra is discussed in Sec. IV together with comparisons to statistical-model predictions. Finally in Sec. V, the conclusions of this study are presented.

## II. EXPERIMENTAL METHODS

Beams of $E/A=11$ MeV $^{60}$Ni projectiles, extracted from the Texas A&M K-500 superconducting cyclotron, impinged on a $^{100}$Mo target of thickness 528 $\mu$g/cm$^{-2}$. A schematic of the experimental apparatus is shown in Fig. 1. Evaporation residues were detected in an annular parallel-plate avalanche gas counter (PPAC) centered around the beam axis with its anode subdivided into seven concentric rings allowing the $\theta$ angle of a residue to be determined. This counter was located 33 cm from the target and subtended all $\theta$ angles from 1.5 to 6.6 °. Evaporation residues were separated from other reaction products by measurements of their energy loss in the gas volume of the PPAC and their time of flight to the PPAC. Evaporation-residue cross sections were normalized with respect to the yield of elastically-scattered projectiles detected in a small Si detector located at an angle of $\theta=9.7°$, which is below the grazing angle for the reaction.

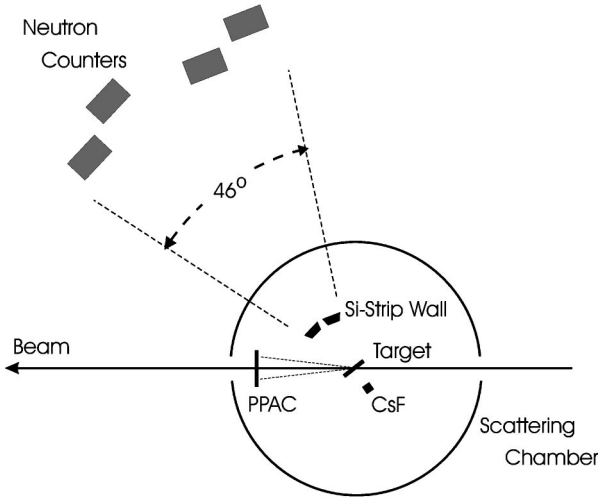


FIG. 1. Schematic indicating the locations of the detectors inside and outside of the scattering chamber.

Light charged particles were detected in a wall of four large-area Si-Si $E-\Delta E$ telescopes located at $\approx$15 cm from the target. The wall covered in-plane angles which ranged from 34° to 80° and an angular range of 32° out of plane. Each telescope consisted of a $\approx$65-$\mu$m-thick Si $\Delta E$ detector followed by a 1-mm-thick Si $E$ detector. The Si detectors, with dimensions of $5\times5$ cm, were each subdivided into 16 strips. For each telescope, the strips on the $E$ and $\Delta E$ detectors were arranged orthogonally, permitting the angular position of a detected particle to be determined to a precision of $\pm0.6°$. The energy calibration of each strip was determined from the measured spectrum of $\alpha$ particles emitted from $^{228}$Th and $^{252}$Cf sources. After correcting for position-dependent Si $\Delta E$ thickness variations ($\pm5\%$), isotope identification of light charged particles ($Z<6$) was obtained from $\Delta E-E$ two-dimensional plots for each telescope. For multihit events in the same telescopes, the identification of all of the particles was often possible (Appendix B).

Sixteen cylindrical-shaped neutron counters were included in the experimental setup at distances of $\approx$110 cm from the target. Four counters were placed behind each Si telescope. The counters, filled with NE213 liquid scintillator, have active diameters of 12 cm. Most of the 16 counters have a thickness of 7.6 cm, except for three of them for which the thickness is 5 cm. The distances from the target to

adjacent counters were offset by the active thickness to reduce neutron scattering between the counters [15]. Neutrons and gamma rays detected in a counter were separated from pulse-shape and time-of-flight information. Standard pulse-shape discrimination techniques measure the time from the start of the light-output pulse to the time at which the differentiated pulse crosses zero. In this work, the total time from the emission of the neutron to the zero-crossing point was measured, which combines both the time-of-flight and pulse-width information. For the same integrated light output, both of these two components are larger for neutrons compared to gamma rays and the resulting $n-\gamma$ separation was excellent. The integrated light output of each neutron counter was calibrated from measurements of the Compton edge associated with detected gamma rays emitted from $^{60}$Co, $^{137}$Cs, and $^{203}$Hg sources. A software threshold of 200 keV was then applied during subsequent data analyses. The detection efficiency of the counters at low neutron energies ($\epsilon < 7$ MeV) was determined using a $^{252}$Cf source placed at the target position. The source was mounted directly on a Si counter which registered each fission event. The detection efficiency was determined as a function of neutron energy from the ratio of the yield of detected coincident neutrons to the values tabulated for $^{252}$Cf in Ref. [16]. Neutron efficiencies were also calculated from the Monte Carlo simulations of Ref. [17]. In the kinetic-energy regime from 4 to 7 MeV, the measured efficiencies were, on average, 8% larger than these calculated values. Therefore for $\epsilon > 7$ MeV, the calculated efficiencies were scaled by 8%.

The target, PPAC, and Si telescopes were located in a thin-walled (3.2 mm Al) spherical scattering chamber of 40 cm radius. From tabulated experimental neutron cross sections [18], the interaction probabilities of neutrons in the walls of the scattering chamber and in the Si telescopes were found negligible, i.e., $\approx 3\%$ and $\approx 1\%$, respectively. The beam was stopped $\approx 9$ m downstream from the target and the background of neutrons from the beam dump was minimal.

Neutron time-of-flight information was measured with respect to a number of reference signals. When the cyclotron rf signal provided this reference, the time of flight was measured with a resolution [full width at half maximum (FWHM)] of $\approx 4$ ns. A CsF scintillator counter (2.5 cm diam$\times$4.0 cm) was placed $\approx 3$ cm from the target. The light output from this counter has a fast rise time and for $\approx 20\%$ of events it detected a gamma ray. Using this signal as the reference, a neutron time-of-flight resolution of $\approx 2.5$ ns was achieved. The CsF detector was also used to determine a ''time-walk'' correction for the Si $E$ and $\Delta E$ detectors. When a fragment ($Z \geqslant 2$) was detected in the Si wall, neutron timing resolution of $\approx 2.5$ ns was also achieved taking the average of the walk-corrected times from the $\Delta E$ and $E$ detectors as the reference. This reference was used in the analysis of the correlations between neutron and charged particles.

## III. RESULTS

### A. Evaporation residues

Evaporation-residue differential cross sections $d\sigma_{\rm ER}/d\theta$ measured in the seven annular rings of the PPAC are plotted against the mean $\theta$ angle of each ring in Fig. 2. The bulk of the evaporation residues are clearly intercepted by the PPAC. The solid curve connects the experimental points and the dashed curve indicates an extrapolation assuming $d\sigma_{\rm ER}/d\Omega$ decreases exponentially at larger angles. This was found to be a reasonable approximation in Refs. [9,19]. From this extrapolation, it is estimated that the PPAC intercepts $\approx 80\%$ of the evaporation residues and consequently, the errors in the total residue cross section associated with the extrapolation are small and the angular bias on the coincidence data is minimal.

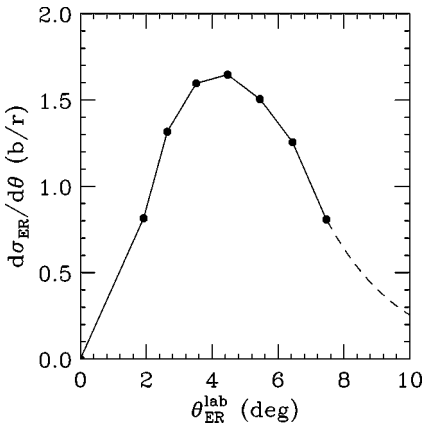


FIG. 2. Experimental angular distribution of evaporation residues. The solid curve connects the experimental points. The statistical error bars are smaller than the plotted data points. The dashed curve shows an exponential extrapolation of the data to larger angles.

The total cross section is plotted in Fig. 3 together with experimental data from the same reaction at lower bombarding energies [19]. The cross sections decrease with increasing bombarding energy and at the higher energies are consistent with the same maximum $l$ wave. This is indicated by the curve which shows the cross section associated with all $l$ waves less than 63 $\hbar$.

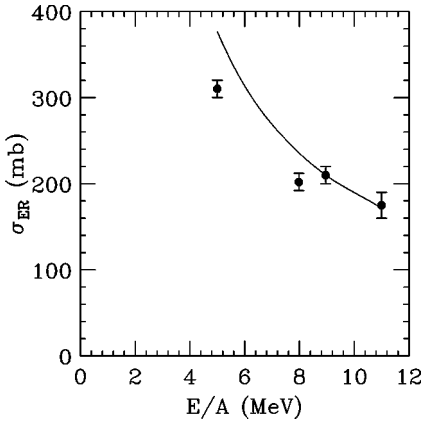


FIG. 3. Experimental evaporation-residue cross sections plotted against the beam energy per nucleon. The highest-energy point was obtained in the present study and the lower-energy points are from Ref. [19]. The solid curve indicates the cross section associated with all partial waves with angular momentum of 63$\hbar$ and less.

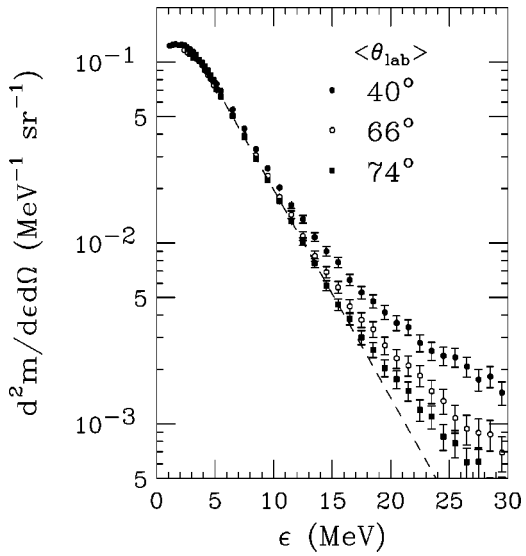


FIG. 4. Experimental neutron-multiplicity kinetic-energy spectra $d^2m/d\epsilon d\Omega$ in the compound-nucleus frame obtained from neutrons detected at the three indicated laboratory angles in coincidence with evaporation residues. The dash curve is a fit to the exponential tail of the more backward-angle spectra and was used when extracting the equilibrium neutron multiplicity.

### B. Neutron spectra and multiplicity

Neutron laboratory kinetic-energy spectra in coincidence with evaporation residues were constructed event by event from the neutron time of flight measured with respect to the cyclotron rf signal. The scattering of neutrons between the counters was found to be minimal, i.e., if a neutron is detected in one of the counters, the probability that any of the neighboring counters also detects a neutron was 3%. These events were not included in the analysis. A background contribution was subtracted from these spectra and they were subsequently smoothed and deconvoluted taking into account the time resolution determined experimentally for the gamma rays and the range of flight distances associated with interactions at various depths in the neutron detector. The fractional change due to this deconvolution and the detector's efficiency were combined to create a laboratory-energy weighting function. This function was subsequently used to weight events when constructing kinetic-energy spectra in the compound-nucleus frame. Examples of the neutron-multiplicity spectra $d^2m/d\epsilon d\Omega$ are shown in Fig. 4 as a function of the neutron energy $\varepsilon$ in the compound-nucleus frame for three mean detection angles. These spectra were obtained using the compound-nucleus velocity measured by Gonin *et al.* [5] (94% linear momentum transfer). A similar procedure was applied to the subset of events for which the time of flight was measured with respect to the CsF detector. As this latter time measurement had significantly better time resolution, the deconvolution step was less important. However, the resulting deconvoluted spectra, obtained from the two time-of-flight measurements, were identical within the statistical errors suggesting the effects of time resolution are effectively removed. For neutron energies less than $\approx 10$ MeV, the spectra are largely independent of angle and consistent with statistical emission from a compound nucleus. The high-energy tails of the spectra have an angular dependence indicating a nonstatistical component.

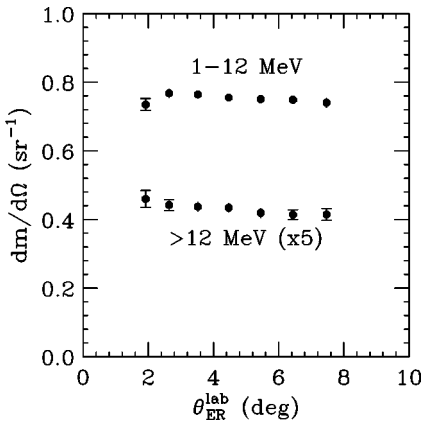


FIG. 5. Experimental dependence of the energy-integrated neutron yield $dm/d\Omega$ for the most forward-angle neutron detectors plotted as a function of the angle at which the evaporation residue is detected. Results are shown for the two indicated neutron kinetic-energy widows of integration.

Due to the limited angular range of the measurement, it is not possible to estimate the integrated multiplicity associated with the nonstatistical contribution, although it is clear in Fig. 4 that this component is small at the measured angles. For the statistical contribution, the multiplicity was estimated from integrating the most forward-angle spectrum in Fig. 4 from 1 to 5 MeV. The contribution from higher energies was obtained from an exponential fit (dashed curve) applied to the most backward angle spectrum from 5 to 12 MeV. The relative contribution from neutron energies below 1 MeV was estimated from statistical model calculations (Fig. 31). However, it comprises only $\approx 10\%$ of the total multiplicity and thus does not need to be determined to high accuracy. The total multiplicity (statistical) obtained from this procedure is $10.4 \pm 1.2$. The largest contribution to the error bar arises from uncertainties in the efficiencies of the neutron counters. This multiplicity is smaller than the value of $14.80 \pm 0.5$ measured for the same reaction by Gonin *et al.* [5,13] for evaporation residues detected at $\theta_{ER}^{lab} \approx 0°$. Although the extracted multiplicities are different, the shape of the neutron spectra are consistent. The dependence of the multiplicity on residue angle $\theta_{ER}^{lab}$ is very small, this is illustrated in Fig. 5 where the integrated yield $dm/d\Omega$ of the most forward-angle spectrum in Fig. 4 is plotted against the detected residue angle for neutron energy windows of $1 < \epsilon < 12$ MeV and $\epsilon > 12$ MeV. These two windows are dominated by the statistical and nonstatistical components, respectively. However, for both windows, there is almost no observed dependence of the integrated yield on the detected residue angle. Thus the present multiplicity measurement is difficult to reconcile with the zero-degree result of Ref. [5].

### C. Charged particle spectra and multiplicities

Kinetic-energy spectra of charged particles detected in coincidence with evaporation residues were transformed event

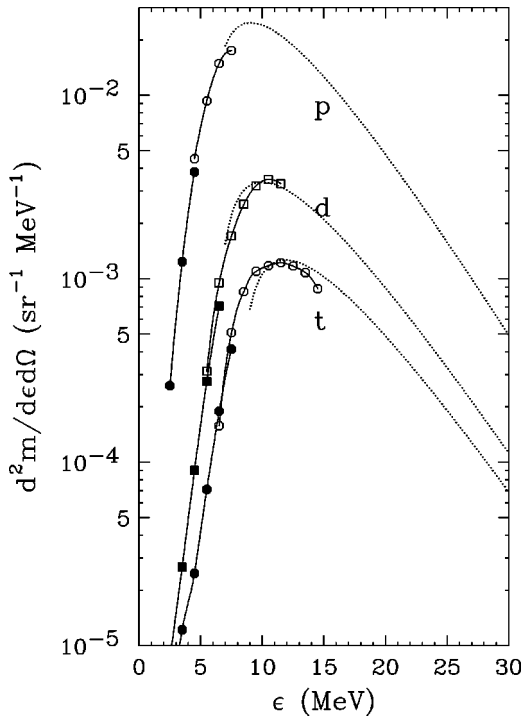


FIG. 6. Experimental kinetic-energy spectra $d^2m/d\epsilon d\Omega$ (in the compound-nucleus frame) of protons, deuterons, and tritons detected in coincidence with evaporated residues. Results obtained with the two forward-angle Si telescopes are indicated by the solid data points, while the open data points were obtained from the two backward-angle telescopes. The solid curves connect these data points. The dotted curves are fits to the equivalent spectra measured by Gonin *et al.* [13], where the multiplicities have been increased by a factor of 2.3 to match the experimental data of this work.

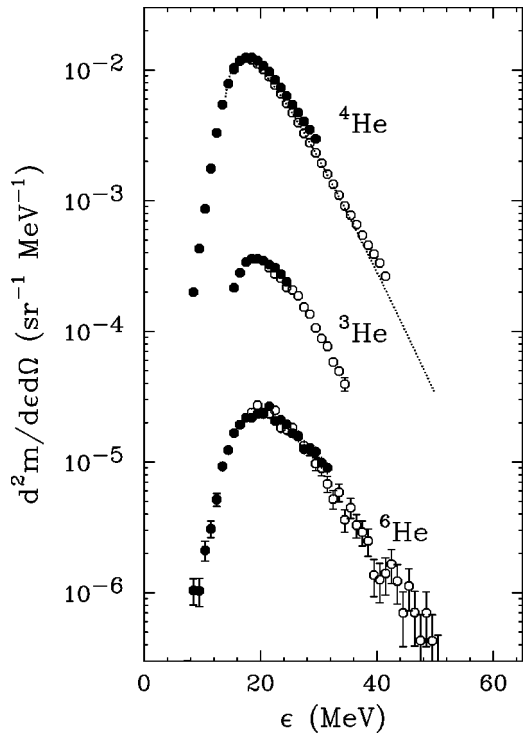


FIG. 7. As for Fig. 6, but for the He isotopes. The dotted curve is the fit obtained by Gonin *et al.* [5] to their measured $\alpha$-particle spectra. It has been normalized to fit the data of this work.

by event into the compound-nucleus frame. Spectra obtained for H, He, Li, and Be isotopes are shown in Figs. 6–9, respectively. The spectra indicated by the filled data points were obtained from particles detected in the more forward-angle Si telescopes ($\langle\theta^{\rm lab}\rangle \approx 45°$), while the open data points are associated with the more backward-angle telescopes ($\langle\theta^{\rm lab}\rangle \approx 70°$). Some of the spectra are severely restricted in kinetic energy due to the thresholds associated with particle identification. This is especially the case for protons for which only the lowest energies are stopped in the Si $E$ detector. The threshold associated with stopping in the Si $E$ detector is important for all hydrogen and helium isotopes at more forward angles. The low-energy threshold for particle identification occurs when particles stop in the Si $\Delta E$ detectors. This threshold restricts the spectra for all particles detected in the more backward-angle telescopes.

For the hydrogen isotopes, it is impossible, from the restricted measurements, to estimate the integrated multiplicities. The data are compared in Fig. 6 to fits of the corresponding spectra measured in the work of Gonin *et al.* [5] (dotted curves). The normalizations of these fits were adjusted to match the experimental $d$ and $t$ data of the present work and correspond to multiplicities which are a factor of 2.3 larger than the values obtained in Ref. [5]. The same factor is used for the protons as there is not sufficient overlap between the data and the fit to make an accurate match.

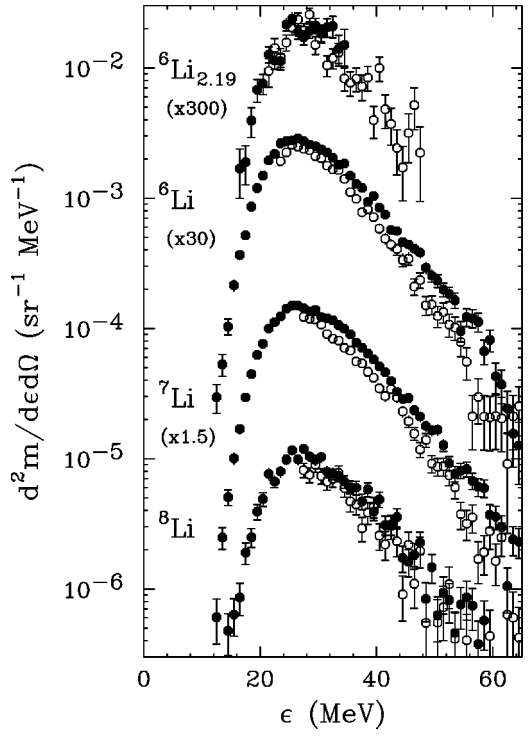


FIG. 8. As for Fig. 6, but for the Li isotopes. Results are also given for the $^6$Li excited state ($E^*=2.19$ MeV) which was reconstructed from $d-\alpha$ pairs. For display purposes, the spectra have been shifted along the $y$ axis by the indicated amounts.

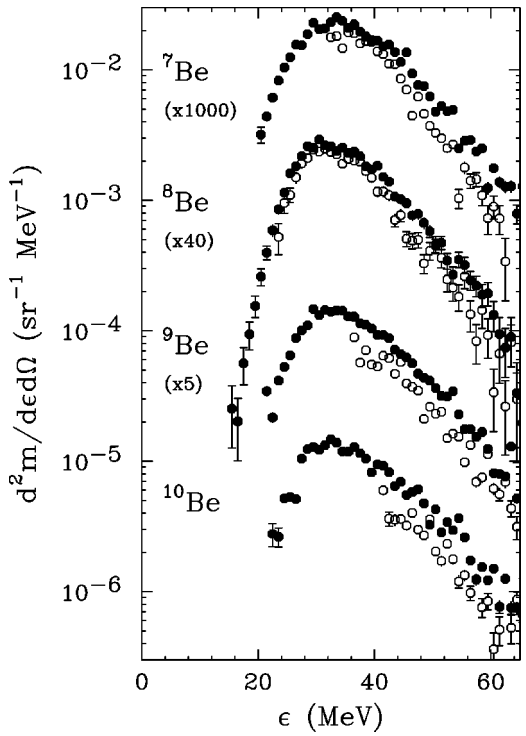


FIG. 9. As for Fig. 6, but for Be isotopes. Results are also given for the unstable $^{8}$Be ground state, which was reconstructed from $\alpha-\alpha$ pairs. For display purposes, the spectra have been shifted along the *y* axis by the indicated amounts.

Gonin *et al*. [5] report that the $\alpha$-particle spectrum measured at $\theta^{\rm lab}=30°$ shows a small nonstatistical component. A consistent result is found in the present work as the slope of the spectra at 30 MeV is somewhat harder in the forward-angle compared to the backward-angle telescopes, as shown in Fig. 7. Also the shape of the statistical component fit by Gonin *et al*. (dotted curve) is in excellent agreement with the spectrum measured in the more backward-angle telescopes. Similar agreement is also obtained with the spectrum measured in the reaction $E/A=10$ MeV $^{64}$Ni+$^{100}$Mo [9]. The experimental angular distribution $dm/d\Omega$ as a function of the angle $\theta_\alpha^{\rm CN}$ in the compound-nucleus frame for the kinetic-energy window of 15–20 MeV is plotted in Fig. 10. This angular distribution, which should be dominated by the statistical component, appears to show a small angular anisotropy, although our sensitivity to it is not great due to the limited angular range of the experiment. The solid curve in Fig. 10 shows a fit to the data using the sum of zeroth- and second-order Legendre polynomial terms. This angular dependence is assumed at all energies to integrate the multiplicity of the statistical component. However, a fit with a constant $dm/d\Omega$ gives a multiplicity which is only 6% smaller than the reported value. Taking the energy dependence from the forward-angle telescopes at low energies and from the more backward-angle telescopes at high energies, an average statistical multiplicity of $1.9\pm0.1$ is obtained for all detected evaporation residues. The dependence of this multiplicity on the detected residue angle is shown in Fig. 11. Due to the larger recoil momentum associated with emitting an $\alpha$ particle, its multiplicity, unlike the neutron multiplicity, is more strongly correlated with the angle of the evaporation residue. The result from the zero-degree study of Gonin *et al.* is also indicated. The rms multiple-scattering angle of evaporation residues in the target material, estimated from the TRIM code [20], is 0.8°. A similar value is also estimated for the work of Gonin *et al.* With multiple scattering of such magnitude, it appears difficult to reconcile our measured angular dependence with the result of Gonin *et al.* To further emphasize this point, the results of the GEMINI statistical-model simulation (calculation with deformation in Sec. IV B) including the effects of multiple scattering are indicated by the solid curve. This curve illustrates that no large dependence of the $\alpha$-particle multiplicity on residue angle is expected for $\theta_{\rm ER}^{\rm lab}<3°$. Therefore the $\alpha$-particle multiplicity, like those for the hydrogen isotopes discussed previously, are larger in the present study than those of Ref. [5].

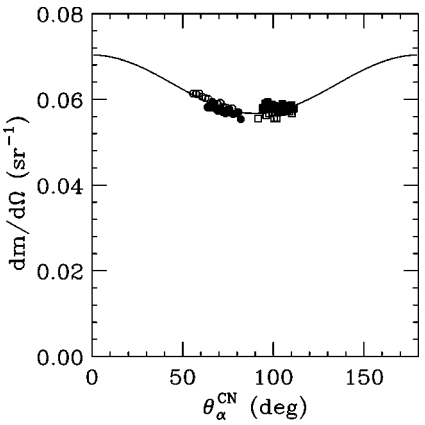


FIG. 10. Experimental angular distribution of the $\alpha$-particle yield in the compound-nucleus frame for kinetic energies from 15 to 20 MeV. Circular and square data points are from the more forward- and backward-angle telescopes, respectively. Solid and open data points are from the in- and out-of-plane telescopes, respectively. The curve displays a fit to the data.

Figures 8 and 9 show the spectra for Li and Be isotopes, respectively. It is found, that for each element, the spectral shapes are almost independent of the mass number *A*. All the

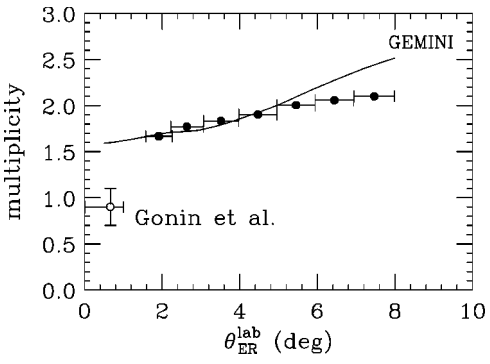


FIG. 11. Experimental statistical $\alpha$-particle multiplicities extracted as a function of the detection angle of the evaporation residue. The result from the study of Gonin *et al.* [13] is indicated. The solid curve shows the dependence predicted by the GEMINI statistical-model calculations.

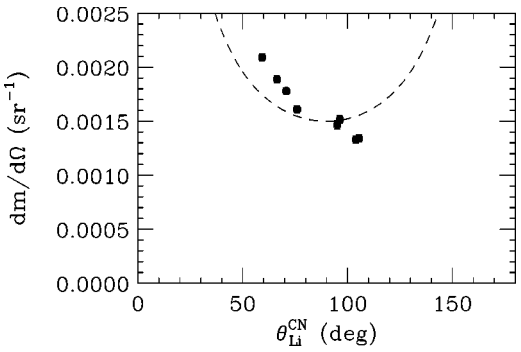


FIG. 12. Angular distribution of $^{7}$Li fragments in the compound-nucleus frame with kinetic energy above 27 MeV detected in coincidence with evaporation residues. For comparison, the curve indicates a distribution with a $1/\sin\theta$ dependence.

charged particle spectra in Figs. 7–9 are evaporationlike, i.e., Coulomb shifted with exponentially decreasing tails. However, the tails of the kinetic-energy spectra show angular dependencies with the largest yields at the more forward angles. This behavior is not consistent with a purely statistical emission as illustrated in Fig. 12, where the angular distribution of the integrated yield in the tail ($\epsilon > 27$ MeV) of the $^{7}$Li spectra is shown. The shape of this angular distribution is typical of that obtained for the other isotopes. The statistical component should be symmetric about 90° and the angular dependence should be no stronger than a $1/\sin\theta$ variation, which is indicated by the dashed curve. The experimental angular distribution of the tail clearly rises faster than a $1/\sin\theta$ variation at forward angles and does not appear to display any symmetry around 90°. Thus, the Li and Be isotopes also have nonstatistical components qualitatively similar to the results obtained for deuterons and tritons emitted in $^{64}$Ni+$^{100}$Mo reactions [9] and for light intermediate mass fragments in Refs. [21,22]. Without more extensive angular distributions, it is difficult to obtain accurate multiplicities for both the statistical and nonstatistical components. However, if the nonstatistical component is minimal for the more backward-angle telescopes, then we can estimate the statistical multiplicity, in a manner similar to that for the $\alpha$ particles, by taking the energy dependence of the statistical component from the forward-angle telescopes at low energies and from the more backward-angle telescopes at high energies. The angular distributions have been assumed isotropic in these estimates. For $\alpha$ particles this was a reasonable assumption, but the anisotropy of the angular distributions may be stronger for heavier fragments. The experimental multiplicities are listed in Table I together with the statistical uncertainties. It is difficult to estimate all the systematic uncertainties on the absolute values. However, the systematic uncertainties are reduced when one is considering the relative yields of the fragments in the measured angular range. In any case, the resulting multiplicities are exceedingly small for all of these isotopes.

### D. Particle-unstable fragments

The presence of particle-unstable fragments can be discerned from the correlations between the decay products.

TABLE I. Experimental multiplicities of evaporated particles detected in coincidence with evaporation residues. Particle-unstable fragments are indicated by an asterisk.

| Particle | Multiplicity |
|---|---|
| $n$ | $10.2 \pm 0.7$ |
| $^{3}$He (g.s.) | $0.053 \pm 0.011$ |
| $\alpha$ | $1.9 \pm 0.1$ |
| $^{5}$He (g.s.)* | $0.14 \pm 0.04$ |
| $^{6}$He (g.s.) | $0.0046 \pm 0.0007$ |
| $^{7}$He (g.s.)* | $0.0005 \pm 0.0003$ |
| $^{5}$Li (g.s.)* | $0.066 \pm 0.033$ |
| $^{6}$Li (g.s.) | $0.018 \pm 0.002$ |
| $^{6}$Li (2.19 MeV)* | $0.016 \pm 0.002$ |
| $^{7}$Li (g.s.) | $0.020 \pm 0.002$ |
| $^{7}$Li (4.63 MeV)* | $0.0067 \pm 0.0007$ |
| $^{8}$Li (g.s.) | $0.0021 \pm 0.0006$ |
| $^{7}$Be (g.s.) | $0.0036 \pm 0.0010$ |
| $^{7}$Be (4.57 MeV)* | $0.0016 \pm 0.0006$ |
| $^{8}$Be (g.s.)* | $0.014 \pm 0.002$ |
| $^{8}$Be (3.04 MeV)* | $0.032 \pm 0.008$ |
| $^{9}$Be (g.s.) | $0.006 \pm 0.001$ |
| $^{9}$Be (2.43 MeV)* | $0.005 \pm 0.001$ |
| $^{10}$Be (g.s.) | $0.003 \pm 0.001$ |
| $^{9}$B (g.s.)* | $0.0006 \pm 0.0002$ |
| $^{12}$C (7.65 MeV)* | $0.00011 \pm 0.00005$ |
| $^{12}$C (9.64 MeV)* | $0.0007 \pm 0.0003$ |

The evidence for such correlated particles has varying degrees of complexity depending on the number of particles in the exit channel and whether or not the primary fragment decays close to the compound nucleus where the interaction of the decay products with its Coulomb is important.

#### *1. Fragments with two-body exit channels*

Simple examples of long-lived two-body decays are illustrated in Figs. 13–15 for $\alpha-\alpha$, $d-\alpha$, and $t-\alpha$ pairs. In the (a) frames of these figures, the square data points give the experimental distributions of the relative energy $\epsilon_{rel}$ for all such pairs detected in coincidence with evaporation residues. The relative energy is the total kinetic energy of the light particles in their center-of-mass frame. Apart from correlated pairs produced in the decay of particle-unstable parents, there is also a ''background'' of uncorrelated pairs. The greatest contribution to these uncorrelated pairs is where both particles in the pair are directly evaporated by the compound nucleus. The shape of this background is estimated from event mixing, i.e., particle pairs are constructed from particles detected in coincidence with different evaporation residues. The solid curves in the (a) frame of these figures show the background distributions, which have been normalized to fit the experimental distributions at the higher values of $\epsilon_{rel}$. The background-subtracted relative-energy distributions are indicated by the circular data points in the (b) frames of these figures, which all contain a well-defined peak associated with sequential decay of a particle-unstable fragment.

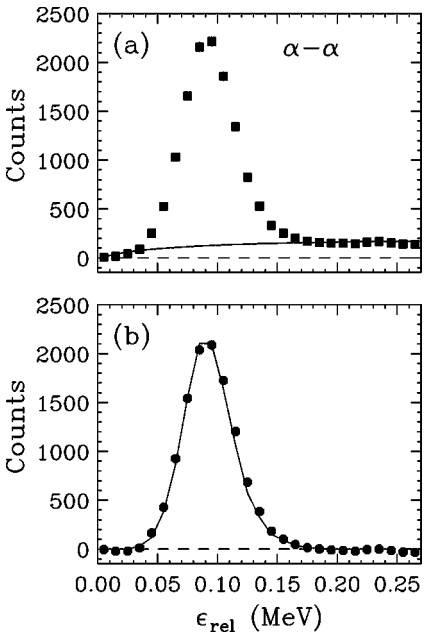


FIG. 13. Relative-energy distributions of $\alpha-\alpha$ pairs detected in coincidence with evaporation residues. (a) The raw distribution is indicated by the square data points. The solid curve gives the estimated background of uncorrelated pairs. (b) The circular data points give the background-subtracted distribution. The solid curve now indicates the predicted distribution of pairs originating from the decay of $^{8}$Be ground-state fragments.

Apart from the correlations of interest, correlations also exist between the particles directly emitted from the compound nucleus due to final-state interactions. For evaporation times predicted for this reaction, the only important final-state interaction between evaporated particles is the long-range Coulomb interaction for which the net effect is a suppression of charged-particle pairs with small relative energy.

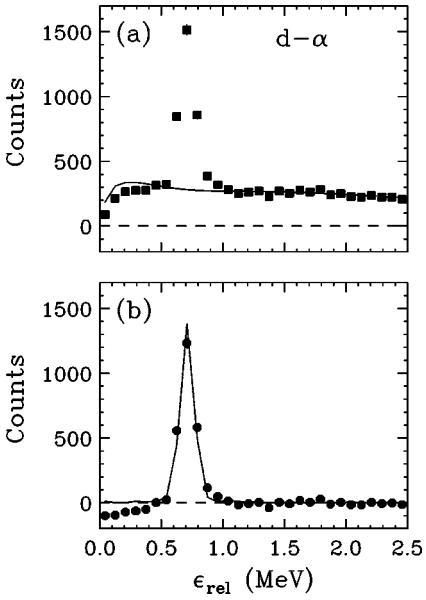


FIG. 14. As for Fig. 13, but now for $d-\alpha$ pairs. The curve in (b) is associated with the decay of $^{6}$Li ($E^{*}=2.19$ MeV) fragments.

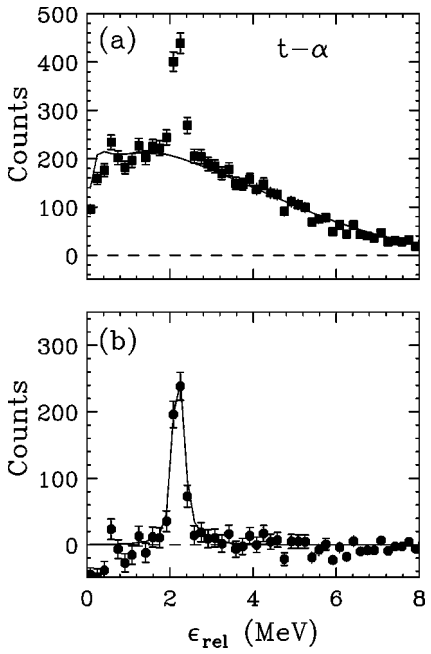


FIG. 15. As for Fig. 13, but now for $t-\alpha$ pairs. The curve in (b) is associated with the decay of $^{7}$Li ($E^{*}=4.63$ MeV) fragments.

For the purposes of this work, it would be better to include the Coulomb suppression in the background contribution so that the background-subtracted spectra contain only the yield from the sequential decay of the particle-unstable fragments. However, this is not done as it is difficult to experimentally determine the magnitude of the Coulomb suppression. As a result, the background-subtracted spectra for the $d-\alpha$ and $t-\alpha$ pairs are negative for the lowest values of $\epsilon_{rel}$. For these pairs, this is not a problem as the relative energy associated with the narrow peaks in the distribution have higher values where the Coulomb suppression is minimal. However, it is a problem for other particle-unstable fragments which will be presented later.

Multiplicities of particle-unstable fragments are estimated by performing Monte Carlo simulations of the evaporation of the parent fragment, its decay, and detection of the decay products. These simulations, which are discussed in detail in Appendix A, take into account the resolution and efficiency of the particle detectors. The simulated relative-energy distributions (with the same binning as the experimental data) are indicated by the solid curves in Figs. 13(b)–15(b) for decay of $^{8}$Be (g.s.), $^{6}$Li ($E^{*}=2.19$ MeV, $J^{\pi}=3^{+}$ state), and $^{7}$Li ($E^{*}=4.63$ MeV, $J^{\pi}=7/2^{-}$ state) fragments, respectively. The curves have been normalized to the experimental data points enabling the multiplicity of the states to be extracted. The statistical multiplicities for these unstable fragments, defined in the same manner as for the stable fragments (Sec. III C), are listed in Table I.

The background contributions to the $\alpha-\alpha$ and $d-\alpha$ correlations are sufficiently small to allow for the reconstruction of the kinetic-energy spectra of the parent fragments. These spectra, included in Figs. 8 and 9, have been background subtracted and are corrected for the efficiency of detecting and identifying the decay products (as determined in the

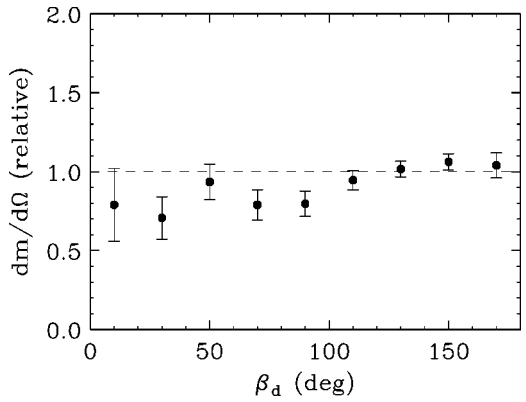


FIG. 16. Experimental angular distribution for the emission of the deuteron from the $^6$Li ($E^*=2.19$ MeV) state. The angle $\beta_d=0$ corresponds to emissions parallel to the velocity vector of the parent $^6$Li fragment in the compound-nucleus frame.

Monte Carlo simulations) as a function of primary-fragment kinetic energy. Within the statistical uncertainties, the spectra determined for the ground and excited states of $^6$Li are identical (Fig. 8). The $^8$Be spectra are also similar to those for the other Be isotopes in Fig. 9 and the high-energy tails have similar angular dependencies. These comparisons clearly suggest that unstable fragments are produced by the same mechanism as the stable fragments.

The parent fragments are assumed to decay isotropically in the Monte Carlo simulations. For the $^6$Li ($E^*=2.19$ MeV, $J^\pi=3^+$) fragment, this may not be the case as statistical emission from high angular-momentum states favor decay channels where the maximum amount of spin is removed from the compound nucleus, i.e., the orbital angular momentum and spin of the emitted particle are both aligned with the compound-nucleus spin. This could be further enhanced if the interaction between the fragment and the daughter compound system has an appreciable spin-orbit term, which would lower the emission barrier when the orbital angular momentum and spin of the fragment are aligned. To search for such an effect, the relative angle $\beta_d$ between the velocity vector of the parent $^6$Li fragment in the compound-nucleus frame and the emission velocity of the deuteron in the frame of this parent $^6$Li nucleus was determined. The background-subtracted efficiency-corrected $\beta_d$ angular distribution is shown in Fig. 16. If there is an appreciable alignment of the particle's spin and orbital angular momentum, then this angular distribution should be symmetric about $\beta_d=90°$ with an overall increase of the yield at smaller and larger $\beta_d$ angles. However, such a dependence is not evident in the experimental angular distribution and hence the alignment is not very large. The experimental angular distribution is consistent with isotropic decay and, if anything, is slightly asymmetric about $\beta_d=90°$, with an enhanced emission of the deuteron backward toward the compound nucleus. The origin of this small effect, if real, is not clear and in any case the assumption of isotropy is clearly sufficient for the purposes of estimating the multiplicities with the Monte Carlo simulations.

Evidence for $^7$He (g.s.) emission is obtained from the experimental $n$-$^6$He relative-energy distribution displayed in

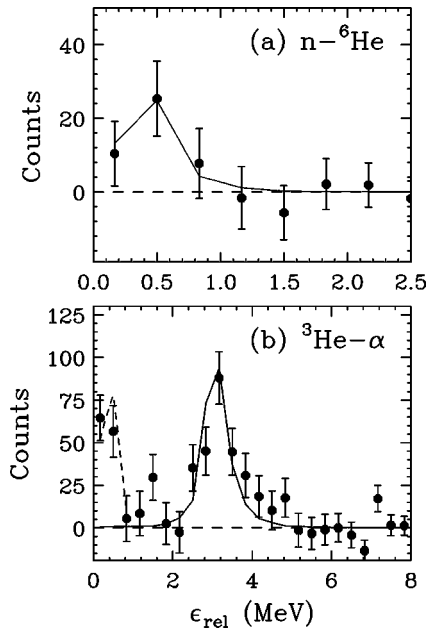


FIG. 17. As for Fig. 13(b), but for (a) $n$-$^6$He pairs and (b) $^3$He-$\alpha$ pairs. The solid curve in (a) is associated with the decay of $^7$He ground-state fragments. In (b), the solid curve is associated with the decay of $^7$Be ($E^*=4.57$ MeV) fragments. The dashed curve is associated with $^8$Be (g.s.) fragments where one of the two $\alpha$ particles from its decay is incorrectly identified as a $^3$He particle.

Fig. 17(a). As there is no Coulomb final-state interaction for these pairs, the background subtraction is expected to be valid even at low values of $\epsilon_{rel}$. The shape of the background-subtracted spectrum is well reproduced by the Monte Carlo simulations, although the statistical errors bars are large.

In Fig. 17(b), two different structures can be identified in the background-subtracted $^3$He-$\alpha$ relative-energy distribution. First, there is a peak at high relative energies ($\epsilon_{rel}\approx 3$ MeV), which can be identified with the $^7$Be ($E^*=4.57$ MeV, $J^\pi=7/2^-$) state. The Monte Carlo simulation of the decay of this state, indicated by the solid curve, is in excellent agreement with data. Second, there is a peak at the lowest relative energies, which has been associated with $^8$Be (g.s.) decay into two $\alpha$ particles. Its presence in this distribution is due to a tail of the intense $\alpha$-particle line in the $E-\Delta E$ map leaking into the neighboring $^3$He line. The dashed curve in Fig. 17(b) indicates the results of a Monte Carlo simulation, which includes this misidentification of an $\alpha$ particle. From the normalization of this curve, it is estimated that $\approx 2\%$ of the particles identified as $^3$He fragments are really $\alpha$ particles in this work.

The sequential decay of $^{10}$B and $^{11}$B states is expected to contribute to the $\alpha$-$^6$Li and $\alpha$-$^7$Li relative-energy distributions, which are shown in Fig. 18. Based on the $\alpha$-$^7$Li correlation function of Ref. [23], where higher statistics permit finer binning of the data, we expected the observed structures to have contributions from a large number of B states. Due to the coarser binning in this work, it is not possible to independently determine multiplicities for each of these states. In the Monte Carlo simulations, the $^{10}$B and $^{11}$B levels are

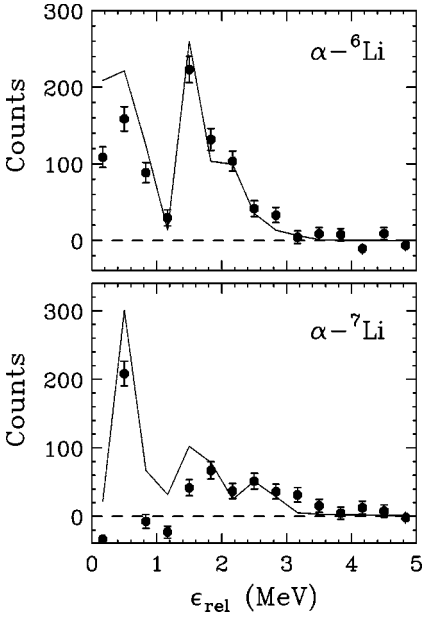


FIG. 18. As for Fig. 13(b), but for $\alpha$-$^6$Li and $\alpha$-$^7$Li pairs. The solid curves are associated with the decay of a thermal distribution of $^{10}$B and $^{11}$B states, respectively, each obtained with a temperature of 3.7 MeV.

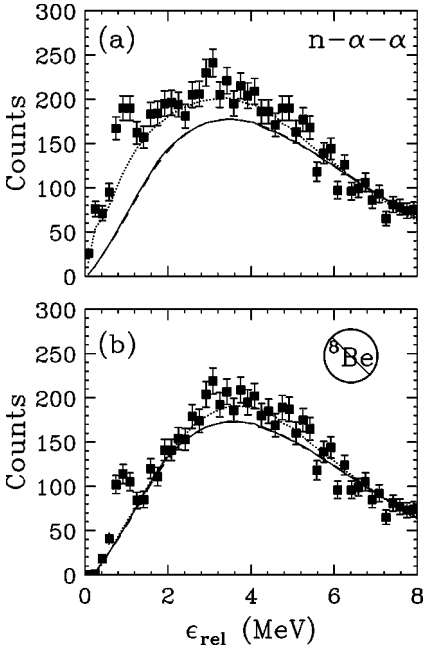


FIG. 19. Relative-energy distributions for $n-\alpha-\alpha$ triplets detected in coincidence with evaporation residues: (a) for all detected triplets and (b) excluding those where the relative energy of the $\alpha-\alpha$ pair is appropriate for $^8$Be (g.s.) decay. The curves indicate background distributions obtained from event mixing. The solid curve is from $(n,\alpha,\alpha)$ mixed events, while the dotted and dashed curves are from $(n,\alpha\alpha)$ and $(n\alpha,\alpha)$ mixed events, respectively (see the text).

assumed to be thermally populated with a temperature of 3.7 MeV (Sec. IV C). These simulations reproduce the overall structure of the background-subtracted spectra. However, there is clearly a problem due to the neglected contribution from the Coulomb final-state interaction in the background distribution as the $\alpha$-$^7$Li spectrum is negative at small values $\epsilon_{\rm rel}$. The $\alpha$-$^6$Li spectrum is probably suppressed at low values of $\epsilon_{\rm rel}$ for the same reason. With this in mind, the normalization for the $^{10}$B simulation is based on the $\alpha$-$^6$Li data points above $\epsilon_{\rm rel}=1$ MeV where this suppression is expected to be minimal. The normalization for the $^{11}$B simulation is more difficult to address as the yield from the $^{11}$B states is smaller at these $\epsilon_{\rm rel}$ values. Therefore, the normalization is based on reproducing the differences between the first three $\alpha$-$^7$Li points. From these normalizations it is estimated that for both $^6$Li and $^7$Li multiplicities, there is an $\approx$13% contribution from decay of these $^{10,11}$B levels.

#### *2. Fragments with three-body exit channels*

A number of unstable fragments which decay into three-body exit channels have been identified in coincidence with evaporation residues. In searching for such decays, care must be taken with the generation of the background distribution. As an illustration of the subtleties of background generation, let us consider the relative-energy distribution for $n-\alpha-\alpha$ triplets plotted in Fig. 19(a). One method of generating the background distribution is to extend the event mixing technique used for the two-body events and create mixed events containing three particles, each from a different event. The background generated from these mixed $(n,\alpha,\alpha)$ events is indicated by the solid curve in Fig. 19(a), which has been normalized to the experimental data at large relative energies ($\epsilon_{\rm rel}>5$ MeV). This background does not reproduce the overall shape of the experimental distribution because it does not contain the strong two-body correlations present in the real data. Therefore the background generated in this fashion is not useful for isolating three-body correlations. The two-body correlations of most importance are associated with $\alpha-\alpha$ pairs produced from the decay of $^8$Be fragments. Contributions from the decay of the ground and first excited states (Secs. III D 1,III D 3) amount to $\approx$20% of all detected $\alpha-\alpha$ pairs. Also, there are two-body correlations associated with Coulomb final-state interactions. All these two-body correlations can be incorporated by creating mixed events from real $\alpha-\alpha$ coincident pairs and a neutron from another event. The background distribution from these mixed $(n,\alpha\alpha)$ events is indicated by the dotted curve in Fig 19(a), which now reproduces the overall shape of the experimental data. However, this background does not contain the $n-\alpha$ two-body correlations. These correlations are of much less importance as the correlated $n-\alpha$ pairs (Sec. III D 3) account for only $\approx$4% of all such pairs. This is further confirmed by noting that the background generated from mixed $(\alpha,n\alpha)$ events, indicated by the dashed curve in Fig. 19(a), is practically identical to the uncorrelated $(n,\alpha,\alpha)$ background.

The $(n,\alpha\alpha)$ background-subtracted distribution is shown in Fig. 20(a). The four lowest excited states of $^9$Be are expected to contribute to this distribution, but these states overlap and, like the $\alpha$-Li distributions, it is impossible to independently determine multiplicities for any of these states from this distribution. However, only one of these states ($E^*=2.43$ MeV, $J^\pi=5/2^-$) does not decay predominately

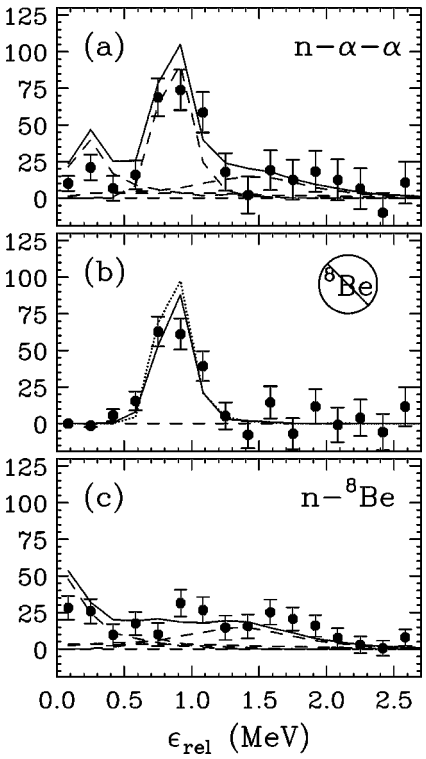


FIG. 20. Background-subtracted relative-energy distributions for $n-\alpha-\alpha$ triplets detected in coincidence with evaporation residues. Results are shown for (a) all detected triplets and (b) only those where the $\alpha-\alpha$ relative energy is greater than 0.2 MeV and hence these $\alpha-\alpha$ pairs cannot originate from the decay of the $^8$Be (g.s.). The curves in (b) show predictions for the decay of the $^9$Be $E^*=2.43$ MeV state. The solid curve was obtained assuming a $^5$He (g.s.) intermediate while for the dotted curve a $^8$Be ($E^*=3.04$ MeV) intermediate was assumed. (c) Relative-energy distribution for neutron plus reconstructed $^8$Be (g.s.) pairs. The solid curves in (a) and (b) are the predictions for a thermal distribution of $^9$Be states with a temperature of 3.7 MeV.

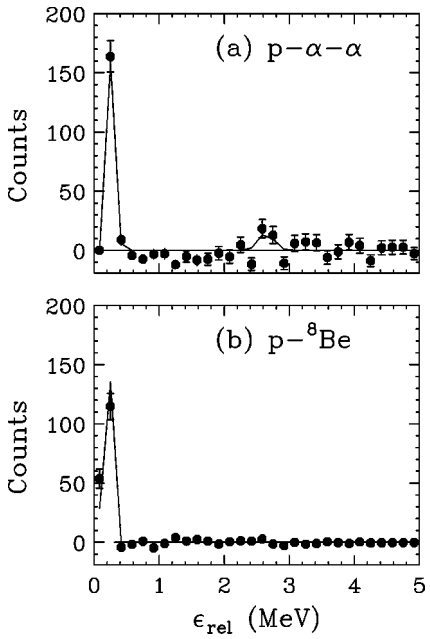


FIG. 21. Background-subtracted relative-energy distributions for $p-\alpha-\alpha$ triplets and $p$-$^8$Be pairs detected in coincidence with evaporation residues. The $^8$Be fragments have been reconstructed from detected $\alpha-\alpha$ pairs. The curves show the predicted distributions for decay of the $^9$B ground state. For the $p-\alpha-\alpha$ triplets, a curve associated with the $E^*=2.36$ MeV excited state is also indicated.

via the $^8$Be (g.s.) intermediate. This state can be isolated by excluding events where the relative energy between the $\alpha-\alpha$ pair is less than 0.2 MeV and hence these $\alpha$ particles cannot originate from a $^8$Be (g.s.) fragment. The relative-energy distribution for such events and the corresponding background distributions are plotted in Fig. 19(b). The differences between the three background distributions are now diminished as a large fraction of the correlated $\alpha-\alpha$ pairs have been removed. The $(n,\alpha\alpha)$ background-subtracted distribution is plotted in Fig. 20(b) and it contains a well-defined peak whose position is reproduced by the Monte Carlo simulations (curves). Note that in these simulations, the decay of the $E^*=2.43$ MeV state has been simulated both as an $\alpha$ decay through a $^5$He intermediate (solid curve) and as a neutron decay to a $^8$Be ($E^*=3.04$ MeV) intermediate (dotted curve). However, the predicted relative-energy distributions are almost identical in the two simulations so it is not possible to differentiate between these possibilities from the present data.

To better isolate the other $^9$Be states, it useful to reconstruct $^8$Be (g.s.) fragments from the pairs of $\alpha$ particles, which produce the peak in the relative-energy distribution of Fig. 13(b), and from these create the $n$-$^8$Be relative-energy distribution shown in Fig. 20(c). The rejection of the other $\alpha-\alpha$ pairs is important as it reduces the background considerably. The ($E^*=1.68$ MeV, $J^\pi=1/2^+$), ($E^*=2.78$, $J^\pi=1/2^-$), and ($E^*=3.05$, $J^\pi=5/2^+$) $^9$Be states, which decay mainly through $^8$Be (g.s.) are all wide ($\Gamma>200$ keV) and still cannot be individually resolved. The prediction for a thermal distribution (temperature$=3.7$ MeV) of these $^9$Be states is indicated by the solid curve in Fig. 20(c), where the normalization of the curve is established from the multiplicity of the $E^*=2.43$ MeV state fitted in Fig. 20(b). This distribution is very broad and rather featureless, but it does reproduce the experimental data within the statistical errors.

The $(p,\alpha\alpha)$ background-subtracted $p-\alpha-\alpha$ distribution, shown in Fig. 21(a), is dominated by a peak at very low relative energies associated with the ground state of $^9$B. Given that most protons emitted from the compound nucleus have kinetic energies above the high-energy threshold for particle identification (Sec. III C), one might also expect the probability for detecting the proton from this channel is very small. However, the detection probably is not as small as one might naively expect as the protons from the decay of $^9$B fragments are predicted to have very small kinetic energies ($\approx 5$ MeV) in the compound-nucleus frame (Fig. 29). The $p$-$^8$Be relative-energy distribution, plotted in Fig. 21(b), confirms that $^9$B (g.s.) decays to the $^8$Be (g.s.) intermediate. There is also weak evidence for the $E^*=2.36$ MeV $J^\pi=5/2^-$ state at $\epsilon_{\rm rel}\approx 2.5$ MeV in the $p-\alpha-\alpha$ distribution. This state decays to the $^5$Li intermediate and thus its absence

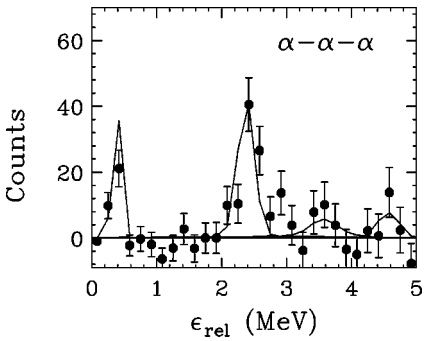


FIG. 22. Background-subtracted relative-energy distributions for $\alpha-\alpha-\alpha$ triplets detected in coincidence with evaporation residues. The curves show the predictions for the decay of a thermal distribution of $^{12}$C states with a temperature of 3.7 MeV.

in the $p$-$^{8}$Be distribution is expected.

The $(\alpha,\alpha\alpha)$ background-subtracted $\alpha-\alpha-\alpha$ distribution, shown in Fig. 22, also shows some structure. Curves indicating Monte Carlo predictions of four $^{12}$C states are indicated. Only the lower two ($E^*=7.65$ MeV, $J^\pi=0^+$ and $E^*=9.64$ MeV, $J^\pi=3^-$) states can be statistically resolved in the experimental distribution.

### *3. Short-lived fragments*

The unstable fragments which contribute most to the $\alpha$-particle yield are $^{5}$He (g.s.) and $^{8}$Be ($E^*=3.04$ MeV, $J^\pi=2^+$). Both fragments are short lived ($\Gamma=0.6$ and 1.5 MeV, respectively) and typically decay in the vicinity of the compound system. The Coulomb field of compound nucleus subsequently modifies the relative energy of the decay products, thus broadening the width of the peak in the relative-energy distribution.

The $\alpha-\alpha$ relative-energy distribution is shown in Fig. 23(a). The low-energy peak associated with $^{8}$Be (g.s.) decay in Fig. 13 is now suppressed in this figure. Before one can isolate this Coulomb effect it is again important to consider the background contribution. Apart from the uncorrelated background there is also a correlated background from the three-body decay of $^{9}$Be ($E^*=2.43$ MeV, $J^\pi=5/2^-$) and $^{12}$C ($E^*=9.6$ MeV, $J^\pi=2^+$) states. The dashed curves in Fig. 23(a) are Monte Carlo predictions of these components using the multiplicities determined from Sec. III D 2. The peak associated with $^{9}$Be is clearly visible in both the raw and background-subtracted spectra in Fig. 23(b) where only the uncorrelated background is subtracted here. The dash curve in Fig. 23(b) is from a Monte Carlo simulation of $^{8}$Be ($E^*=3.04$ MeV) decay ignoring the Coulomb field of the compound nucleus. This curve also includes the small contribution from the decay of $^{12}$C ($E^*=9.6$ MeV), which produces a low-energy shoulder at $\epsilon_{rel}\approx 2$ MeV. However, this prediction fails to reproduce the width of the broad experimental peak in the relative-energy spectrum. Much better agreement is obtained when the simulations were modified to include three-body Coulomb-trajectory calculations to follow the motion of the two $\alpha$ particles and the compound system. The details of these calculations are reported in Appendix A and the resulting relative-energy distribution is shown by the

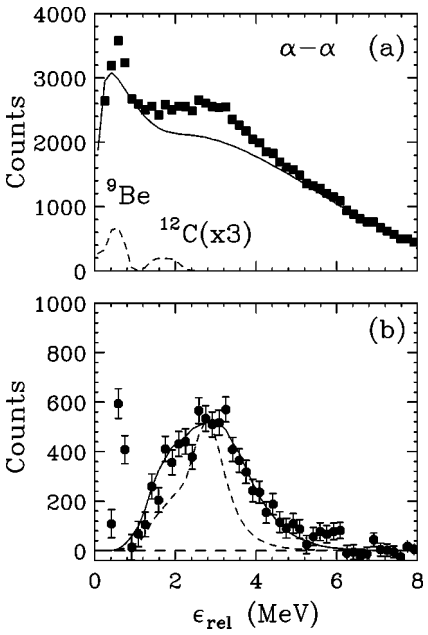


FIG. 23. As in Fig. 13, but results are for larger $\alpha-\alpha$ relative energies. The $^{8}$Be (g.s.) peak evident in the much expanded energy scale of Fig. 13 is suppressed in these plots. Correlated backgrounds from the three-body decay of $^{9}$Be ($E^*=2.43$ MeV) and $^{12}$C ($E^*=9.64$ MeV) are indicated by the dashed curves in (a). Monte Carlo predictions for the decay of the $^{8}$Be ($E^*=3.04$ MeV) state are indicated by the curves in (b). The dashed curve contains modification to the relative $\alpha-\alpha$ kinetic energy by the Coulomb field of compound nucleus while the dashed curve does not. For both curves, the small contribution from the decay of $^{12}$C ($E^*=9.64$ MeV) fragments has been included.

solid curve in Fig. 23(b). The multiplicity extracted for this first excited state of $^{8}$Be is larger than that extracted for the ground state (see Table I).

The effect of the Coulomb interactions between the $\alpha$ particles and the compound nucleus is much more evident when the relative-energy distributions are gated on the emission angle $\beta_\alpha$ of the $\alpha$ particles defined as the angle between the velocity vector of the parent $^{8}$Be fragment in the compound-nucleus frame and the emission velocity of one of the $\alpha$ particles in the frame of this parent $^{8}$Be nucleus. Relative-energy distributions are shown in Fig. 24 for transverse decay ($45°<\beta_\alpha<135°$) by the solid data points and for longitudinal decay ($\beta_\alpha<45°$, $\beta_\alpha>135°$) by the open data points. The experimental data are also gated on the kinetic energy defined in the compound-nucleus frame of the primary $^{8}$Be fragment. The faster this fragment travels, the further it decays, on average, from the compound nucleus and hence the smaller the subsequent modification by the then-weaker Coulomb field. The experimental distributions clearly show that the transverse decay peak (solid points) is shifted toward higher relative energies compared to that for longitudinal decay (open points). As expected, this shift decreases for larger $^{8}$Be kinetic energies. The predictions of the three-body Coulomb-trajectory simulations are indicated by the solid curves in this figure. While these predictions reproduce the experimental trends qualitatively, the predicted

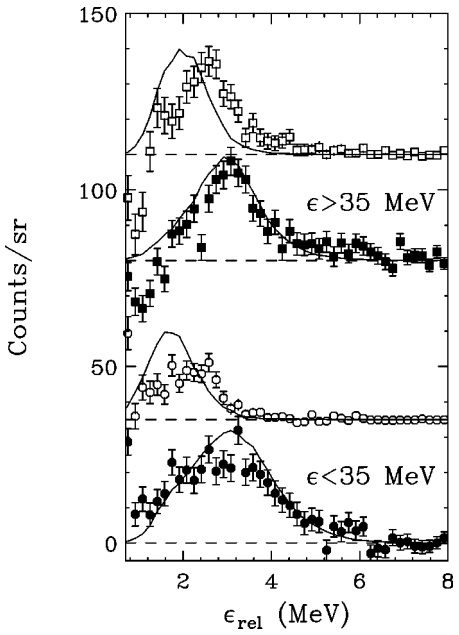


FIG. 24. Experimental $\alpha-\alpha$ relative-energy distribution (background subtracted) gated on the emission angle $\beta_\alpha$ of the $\alpha$ particles from the reconstructed parent $^8$Be fragment and on the kinetic energy $\epsilon$ of this parent fragment in the compound-nucleus frame. The filled data points are obtained for transverse emission of the $\alpha$ particles ($45°<\beta_\alpha<135°$) and the open symbols for longitudinal emission ($\beta_\alpha<45°$, $\beta_\alpha>135°$). The curves indicate the results of Coulomb trajectory simulations of $^8$Be decay in the proximity of the compound nucleus. The data and curves have been shifted along the *y* axis for clarity.

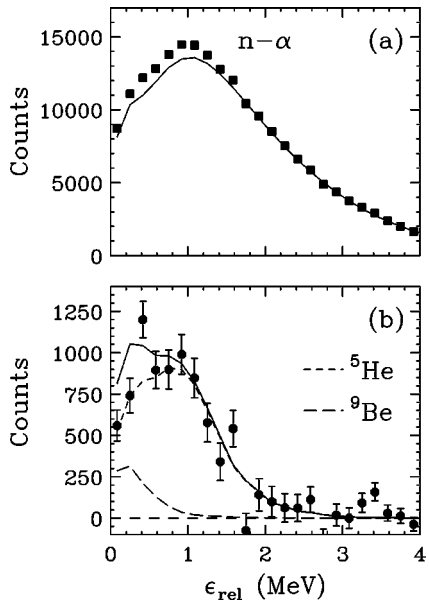


FIG. 25. As in Fig. 13, but for $n-\alpha$ pairs. The curves in (b) show the predicted total (solid) and the indicated contributions from the decay of $^5$He (g.s.) and all $^9$Be states.

magnitude of the shift is larger than that observed experimentally. The explanation for the shift is most easily described in terms of tidal forces. For a uniform Coulomb field, the velocities of both $\alpha$ particles will be modified identically with no ensuing change in their relative energy. However, it is the nonuniform nature of the Coulomb field that is responsible for the observed shift. If the uniform component of the Coulomb field is subtracted, then the resulting tidal field remains [24]. These tidal forces are opposite in sign to the more familiar gravitational tidal force as we have a repulsive instead of an attractive interaction. Hence in the longitudinal direction, the tidal force pushes the $\alpha$ particles together decreasing their relative energy, while in the transverse direction the tidal force pulls them apart increasing their relative energy.

The decay width of a $^5$He (g.s.) fragment is less than half of that for a $^8$Be ($E^*=3.04$ MeV) fragment and hence, on average, it decays in a region where the magnitude of the Coulomb field is weaker. However, the subsequent modification of the relative energy of the $n-\alpha$ decay products is not significantly smaller as now its decay products have different $Z/A$ ratios and experience different accelerations by the Coulomb field. This differential acceleration produces effects which are larger than those from the tidal accelerations. In fact the neutron is not affected by the Coulomb field at all, while the $\alpha$ particle is accelerated. Subsequently if the $\alpha$ particle is emitted in the forward direction, then its Coulomb acceleration increases the $n-\alpha$ relative energy. On the other hand, if the $\alpha$ particle is emitted backwards, then the relative energy is decreased.

Before looking for such effects, it is again important to consider the correlated background from three-body decays. The raw and background (uncorrelated)-subtracted $n-\alpha$ relative-energy distribution in coincidence with evaporation residues is shown in Fig. 25. Note that the uncorrelated background [curve in Fig. 25(a)] is relatively large for this channel. In Fig. 25(b) the contribution from the decay of all $^9$Be states (see Fig. 20) is shown by the indicated curve. However, the absolute yield of these states is not well determined. Contributions from the decay of the $E^*=1.80$ MeV first-excited state of $^6$He will populate the same relative-energy region as these $^9$Be states, but its magnitude has not been experimentally determined. The total $n-\alpha$ distribution in Fig. 25(b) has been fit (solid curve) by normalizing the predicted $^5$He (g.s.) contribution (including Coulomb effects) in the region $\epsilon>1$ MeV where these other background contributions are minimal. Although the resulting sum of both the $^5$He and $^9$Be contributions in Fig. 25 (solid curve) leaves little room for any appreciable contribution from the $^6$He component, it is difficult to exclude some contribution from this state due to the poorly determined $^9$Be yield. The dependence of the background-subtracted relative-energy distribution on the emission angle $\beta_n$ of the neutron from the $^5$He parent is shown in Fig. 26. There is a steady increase of the average relative energy in going from forward ($\beta_n<45°$) to backward ($\beta_n>135°$) neutron emission, as expected. The dash curve indicates the behavior predicted with the Coulomb-trajectory calculations for $^5$He decay. The solid curve also includes the contributions from the decay of the $^9$Be states and reproduces the important features of the experimental data.

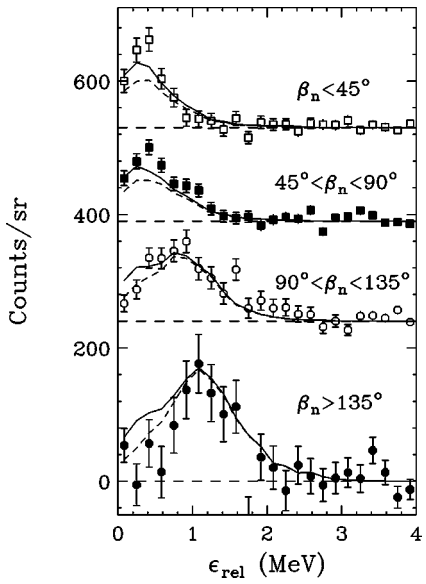


FIG. 26. Background-subtracted $n-\alpha$ relative-energy distributions gated on the emission angle $\beta_n$ of the neutron relative to the direction of travel of the reconstructed $^5$He parent. For clarity the distributions have been shifted along the $y$ axis to separate them. The dashed curves indicate the results of Coulomb-trajectory simulations of $^5$He decay in proximity of the compound nucleus. The solid curves also include the predicted yield from the decay of $^9$Be excited states.

The decay of $^5$Li (g.s.) is expected to have even larger Coulomb effects as both its decay width is very large (1.5 MeV) and its decay products have different $Z/A$ ratios. The raw and background-subtracted $p-\alpha$ relative-energy distributions are displayed in Fig. 27 together with the correlated background predicted from the three-body decay of $^9$B. There is clearly a broad peak in the experimental data which can be associated with $^5$Li (g.s.) decay. Unfortunately the proton's high-energy detection threshold severely distorts this distribution. Detected low-energy $^5$Li protons are mostly produced by backward emission from the parent fragment where the interaction with the Coulomb field of the compound nucleus reduces the relative energy of the $p-\alpha$ pair. The experimental peak is clearly shifted down in energy compared to the 1.96 MeV average relative energy expected

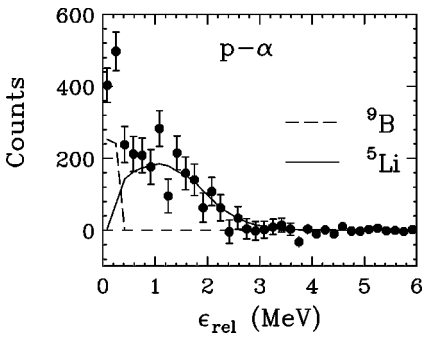


FIG. 27. As in Fig. 13(b), but for $p-\alpha$ pairs. The solid and dashed curves indicate the predicted contribution from the decay of $^9$B (g.s.) and $^5$Li (g.s.) fragments.

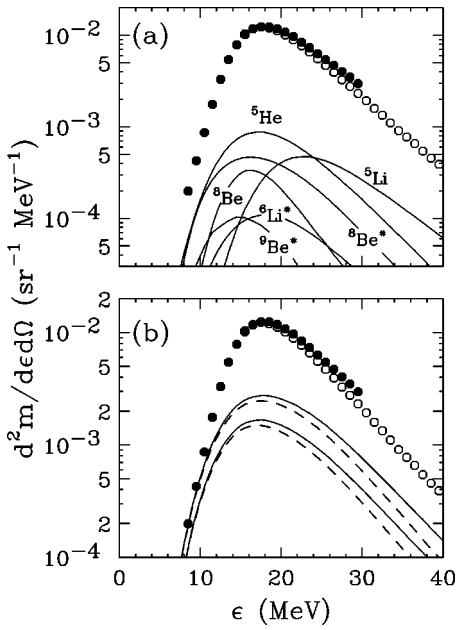


FIG. 28. $\alpha$-particle kinetic-energy spectra. Data points are the experimental results from Fig. 7. (a) The curves indicate predicted contributions to the spectra from each of the identified unstable fragments. The predictions were obtained from the Monte Carlo simulations for the more forward-angle Si telescopes. (b) The solid and dashed curves indicate the total contributions from all identified unstable fragments obtained for the more forward- and backward-angle telescopes, respectively. Two sets of curves are plotted using the maximum and minimum normalization values extracted for each component.

in the absence of such effects. Due to these severe distortions, the error associated with the extracted $^5$Li multiplicity listed in Table I is large.

## IV. DISCUSSION

### A. Influence of sequential decay on kinetic-energy spectra

Experimental multiplicities of stable and unstable fragments detected in coincidence with evaporation residues are listed in Table I. These multiplicities have all been extracted with similar assumptions and hence their relative values are expected to be more accurate than their absolute values. These multiplicities are not exclusive, e.g., the multiplicity associated with $^9$B fragments is also contributing to the multiplicities of its decay products; $^8$Be, $\alpha$, and $p$. Table I indicates that there is a large variety of clusters, besides $\alpha$ particles, emitted from the compound nucleus, albeit at very low multiplicities. As predicted in Ref. [9], $^5$He (g.s.) emission is the most prolific of the particle-unstable fragments. However, its relative yield compared to $\alpha$ particles ($\approx$7%) is significantly lower than the value needed to explain the subbarrier yield in the $\alpha$-particle spectrum in that work ($\approx$30%).

The contribution of the secondary fragments to the experimental kinetic-energy spectra of stable fragments can be estimated from the Monte Carlo simulations (Appendix A). In Fig. 28(a), the simulated $\alpha$-particle spectra for the forward-

angle Si telescopes originating from each of the identified unstable fragments are compared to the experimental spectra. To avoid confusion, the errors associated with the normalization of each of these curves have been omitted. This error is largest for the $^5$Li contribution. However, this fragment does not contribute to the sub-barrier region. Apart from $^5$He, the only other fragment that contributes significantly to the sub-barrier region is $^8$Be ($E^*=3.04$ MeV). The sums of all identified secondary components are plotted in Fig. 28(b) as the solid and dashed curves for the forward and more backward angle telescopes, respectively. Two sets of curves are plotted using the maximum and minimum normalization values extracted for each component. Altogether, $\alpha$ particles from the sequential decay of unstable clusters account for $\approx$14% of all $\alpha$ particles in coincidence with residues. At this level, the important features of the $\alpha$-particle energy spectrum like its peak energy and the slope at large energies are not greatly influenced by the contributions from the identified unstable fragments. However, in the extreme sub-barrier region ($\epsilon<12$ MeV), the simulated sequential contribution dominates the spectrum in Fig. 28(b).

The largest uncertainty in the simulations is in the choice of the initial kinetic-energy distributions of the unstable parents, which are taken from the measured distribution of similar stable isotopes (Appendix A). Simply shifting these assumed distributions up or down in energy will not change our conclusion, i.e., the yield of $\alpha$ particles from sequential decay is simply too small to significantly account for the $\alpha$-particle yield in the peak region. In fact, as the present simulations are already reproducing the yield in the extreme sub-barrier region, one cannot shift the $^5$He and $^8$Be ($E^*$ $=3.04$ MeV) kinetic-energy distributions down in energy. At higher excitation energies the relative contribution of these secondary particles is expected to be larger and they will have a greater influence on the shape of the total kinetic-energy spectrum. The reason for the discrepancy between the experimental spectra and the predictions of standard statistical-model calculations thus lies elsewhere and will be discussed in Sec. IV B.

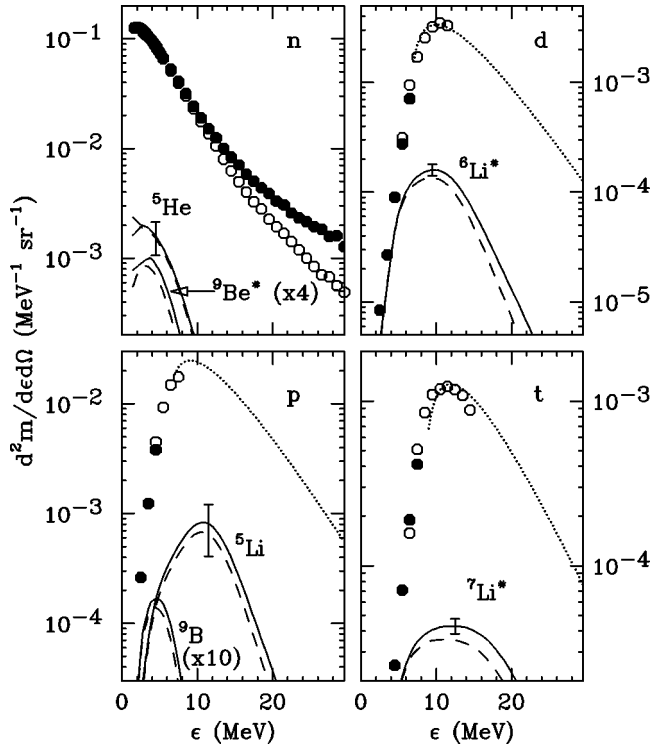


FIG. 29. As for Fig. 28(b), but for neutrons, protons, deuterons, and tritons. The dotted curves are the same as in Fig. 6.

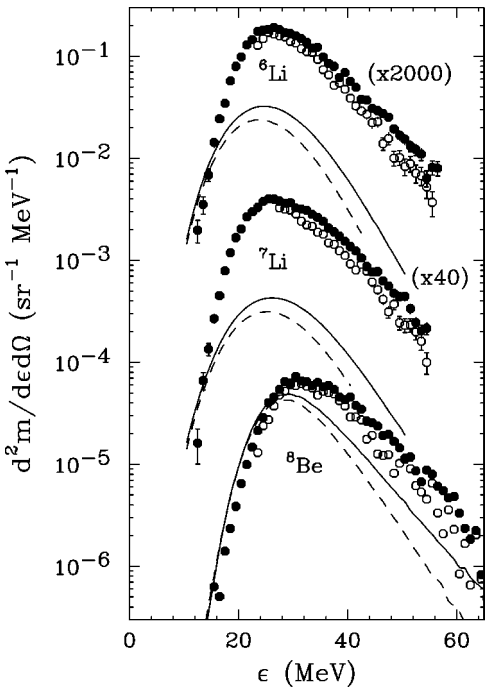


FIG. 30. As in Fig. 28(b), but for $^6$Li, $^7$Li, and $^8$Be fragments. For clarity, the results have been shifted long the *y* axis by the indicated amounts.

As a matter of interest, the identified contributions of secondary fragments to the *n*, *p*, *d*, and *t* spectra are indicated in Fig. 29. Except for the deuterons, these identified contributions are insignificant at all kinetic energies. For deuterons the extreme sub-barrier region also has a significant contribution from sequential decay. In this case the source is $^6$Li ($E^*=2.19$ MeV) fragments. Estimated contributions from sequential decay are also indicated in Fig. 30 for $^6$Li, $^7$Li, and $^8$Be spectra. For both Li spectra, the sequential contributions are from B states for which there is some difficultly in extracting the exact yield due to the lack of Coulomb effects in the background (Sec. III D 1). The sequential contributions plotted for these particles in Fig. 30 are from the same calculations as shown in Fig. 18. Even within these uncertainties, the relative contribution and the enhancement of the sub-barrier region by the sequential component is similar to that obtained for $\alpha$ particles and deuterons. For the $^8$Be spectrum, the important secondary components are from the $E^*=1.68$, 2.78, and 3.05 MeV states of $^9$Be. The $^9$B contribution is insignificant. Again the multiplicity of these $^9$Be states is not well determined (Sec. III D 2) and is possibly overestimated as the simulated secondary component is larger than the experimental data at low energies in Fig. 30. Approximately 50% of the $^8$Be (g.s.) fragments originate

from these $^{9}$Be states in these simulations and the $^{8}$Be spectrum may have the largest distortions from sequential decay.

### B. Statistical-model calculations

Deforming a compound nucleus gives rise to a distribution of Coulomb barriers for the emission of a charged particle. This distribution extends down to lower energies than the spherical barrier and thus enhances the yield of low-energy fragments. If deformation is the major cause of the observed enhancement, then consistent enhancements should be found for all emitted clusters. To investigate this, statistical-model calculations were preformed with the code GEMINI [25]. To begin with, standard calculations with spherical transmission coefficients and rotational energies from the calculations of Sierk [26] are compared to the experimental data. These calculations included the emission and decay (if unstable) of the ground and excited states for all H, He, Li, and Be isotopes. More details of the calculations can be found in Ref. [9] and Appendix C.

As input to these calculations one needs an estimate of the initial excitation energy consistent with the measured average residue velocity, i.e., 94% of the complete fusion value [5]. With the standard incomplete-fusion assumption, i.e., 94% of the projectile's mass fuses with the target and the remaining piece(s) continuing with the beam velocity, an excitation energy of 280 MeV (a reduction of 40 MeV from the complete fusion value) is obtained. However, if there is also mass loss from the target, then more excitation energy can be removed for a given average residue velocity. This is true even for models other than incomplete fusion. Indeed, in the nucleon-exchange transport code [27], where nonstatistical emissions result from nucleons exchanged during the initial contact of the projectile and the target, and which subsequently propagate through and escape from their receptor nucleus, an excitation energy loss of 20 MeV is predicted while the ratio of the residue velocity to the center-of-mass value is only 99.7%. Note also that nonequilibrium neutron emission in fusion reactions is often fit with a thermal source traveling at roughly half the beam velocity [28,29]. The emission of such neutrons has very little effect on the average residue velocity, i.e., the emission of each neutron decreases the residue velocity by only 0.2%. Clearly the excitation-energy loss can be larger for the measured residue velocity than the above-given estimate. An average excitation energy of $240\pm27$ MeV is estimated from energy-balance considerations using the measured multiplicities and average kinetic energies of the evaporated particles. For the hydrogen isotopes, these quantities were taken from Gonin *et al.* [5], but where the multiplicities were increased by a factor of 2.3 (Sec. III C).

Calculations were performed for an excitation energy of 240 MeV and a temperature-dependent level-density parameter of the form used by Fineman *et al.* [8]:

$$a=\frac{A}{8+\kappa\frac{U}{A}}, \tag{1}$$

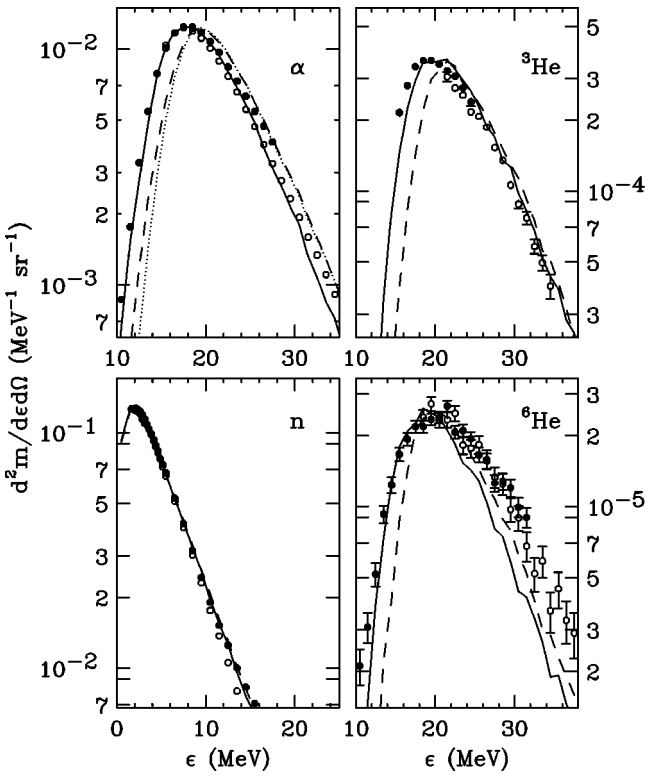


FIG. 31. Comparison of experimental $\alpha$, $n$, $^{3}$He, and $^{6}$He kinetic-energy spectra with statistical model predictions. The dashed and solid curves indicate the predicted results obtained in simulations with spherical and deformed compound systems, respectively. The normalization of the curves was chosen to reproduce the experimental maximum value. The dotted curve indicates the shape of the spectrum for directly emitted $\alpha$ particles predicted in the calculations for spherical compound nuclei.

where $\kappa=1.5$ was chosen to reproduce the slopes of the high-energy tails in both the neutron and the $\alpha$-particle kinetic-energy spectra (see the following) and $U$ is the thermal excitation energy. However, the relative sub-barrier yield obtained from these calculations is not greatly sensitive to the exact value of the excitation energy and level-density parameter. Fission parameters were adjusted to reproduce our measured evaporation-residue cross section.

Predicted kinetic-energy spectra (dashed curves) are compared to experimental data in Figs. 31 and 32. To focus our attention on differences in shape, the predicted and experimental spectra have been normalized to give the same maximum value as the experimental data from the forward-angle telescopes (solid data points). The predicted $^{8}$Be spectrum in Fig. 32 has a significant low-energy shoulder from the sequential decay of $^{9}$Be states as suggested experimentally in Sec. IV A. The GEMINI simulations do not include the post-breakup modification to the kinetic energy from the Coulomb field of the compound nucleus. For the $^{5}$He contribution, the largest source of secondary $\alpha$ particles, it is estimated that this effect increases the simulated $\alpha$ particle energy by 1 MeV on average [9]. Hence for this contribution, the kinetic energies were shifted by this amount. For comparison the dotted curve in Fig. 31 shows the spectrum predicted for directly emitted $\alpha$ particles. The inclusion of

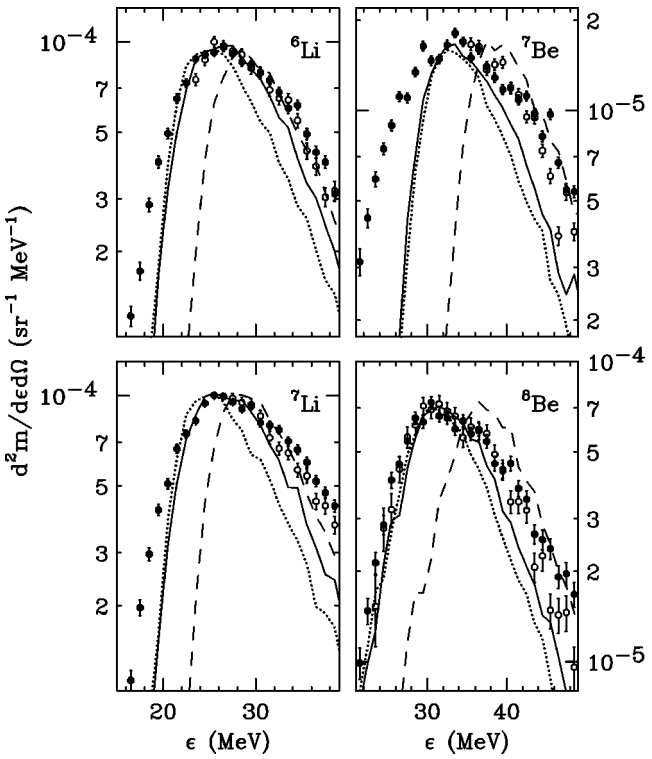


FIG. 32. Same as for Fig. 31, but for $^6$Li, $^7$Li, $^7$Be, and $^8$Be fragments. The dotted curves are from calculations where the Coulomb barrier of each fragment was lowered by increasing the radius parameters of the nuclear potentials by the factor 1.25.

the secondary $\alpha$ particles does enhance the predicted sub-barrier region in these calculations, but not by very much and certainly it is not enough to reproduce the experimental spectra. Further enhancement can be obtained by decreasing the Coulomb barrier for $^5$He emission, but already in these simulations the relative contribution from $^5$He decay is too large by a factor of 1.3–2.6. It is therefore necessary to investigate other mechanisms to explain this sub-barrier enhancement. In fact for all charged particles, the simulations underpredict the relative yield in the sub-barrier region. The magnitude of this effect increases with the $Z$ of the emitted fragment and is quite large for the Li and Be fragments in Fig. 32. Clearly a mechanism common to all fragments is needed to explain this result.

A complete statistical treatment of compound-nucleus decay should consider the equilibrium distribution of compound-nucleus shapes. These distributions have long tails that extend to highly deformed prolate shapes that are a major source of the low-energy particles. Statistical-model calculations including only spheroidal-shape fluctuations predict the correct shape of the $\alpha$-particle kinetic-energy spectrum at low excitation energies ($\approx$100 MeV or less) [11]. Similar calculations including all the evaporation channels of interest in this work are too time consuming. However, in Ref. [11] they were not able to reproduce the relative sub-barrier yield for $\alpha$ particles in the neighboring $E/A=10$ MeV $^{64}$Ni+$^{100}$Mo reaction. It was suggested that either (1) other shape degrees of freedom which are excited at higher excitation energies might contribute to an increased probability of larger deformations, or alternatively (2) at high enough excitation energies, evaporation is expected to commence before the equilibrium distribution of shapes is attained. The evaporation spectra should therefore reflect deformations more similar to the initial shape of the fused system after most of the initial kinetic energy in the reaction has been dissipated [11]. The HICOL dynamical code [30] predicts that this initial dissipation period is very short ($<$0.5 zs), after which the system has a large deformation with a relative quadrupole moment of $Q\approx1.9$ with only a small dependence on impact parameter. Subsequently the shape evolves slowly in time. Both scenarios lead to an increased probability for small Coulomb barriers further enhancing the number of low-energy charged particles. However in scenario (2) this effect is entrance-channel dependent, i.e., for more asymmetric entrance channels the initial deformation should be smaller and the magnitude of the enhancement should decrease while for scenario (1) the effect should be independent of entrance channel.

Experimentally, evidence for entrance-channel dependencies on the shape of the $\alpha$-particle spectrum is conflicting. Cinausero *et al.* [31] report no significant difference in the shape of the $\alpha$ spectra measured in $^{86}$Kr+$^{76}$Ge, $^{16}$O+$^{150}$Sm, and the reaction of this study, all matched approximately in excitation energy. Also Boger *et al.* [7] obtained a similar conclusion for matched $^{40}$Ar+$^{nat}$Ag and $^{86}$Kr+$^{63}$Cu reactions. On the other hand, for a lower excitation energy of 170 MeV, a small enhancement of the low-energy $\alpha$-particle yield was found for the $^{64}$Ni+$^{100}$Mo reaction compared to that from the matched $^{16}$O+$^{148}$Sm reaction [9]. Liang *et al.* [10] have reported entrance-channel dependencies on the slope of the high-energy spectral tails in matched $^{12}$C+$^{144}$Sm and Ni+Zr reactions at even lower excitation energy ($E^*\approx113$ MeV) which they find consistent with the HICOL predictions, although no dependence on the sub-barrier region was noted. At even lower excitation energies ($E^*=49$ MeV), entrance-channel dependencies on the high-energy $\gamma$-ray yield near the giant dipole resonance in matched $^{16}$O+$^{148}$Sm and $^{64}$Ni+$^{100}$Mo reactions have been reported [32]. A consistent understanding of these experimental results is lacking as the trends with excitation energy are the opposite to expectation.

Although the mechanism for the enhancement of low-energy Coulomb barriers is not yet established at these excitation energies, it is interesting, as a lowest-order approximation, to examine whether the Coulomb-barrier distribution associated with an initially fixed, highly deformed shape can successfully reproduce the peak energy of all the detected clusters. This shape can roughly be considered to represent in the two scenarios either (1) some average of the Coulomb barrier distribution associated with the thermal distribution of shapes or (2) the initial shape of the compound system after most of the excitation energy has been dissipated. To this end, GEMINI simulations were performed using transmission coefficients and rotational energies appropriate for a fixed prolate deformation of $Q=1.9$ (ratio of major to minor axes $r_1/r_2=1.6$). The transmission coefficients were obtained from averaging spherical coefficients over the surface area of the system (equivalent sphere approximation

[33,34]). After 5 zs, when the excitation energy is $\approx$100 MeV, the calculation was continued with transmission coefficients and rotational energies appropriate for $Q=0.8$ $(r_1/r_2=1.25)$ which reproduced the experimental $\alpha$-particle spectrum for $E^*=101$ MeV $^{164}$Yb compound nuclei measured in Ref. [9]. It is expected that the equilibrium distribution of shapes should be established by this time in scenario (2) [11] and this latter deformation is introduced to mock up the effects of the equilibrium shape distribution at this excitation energy for which the spheroidal-shape calculations of Ref. [11] reproduce this data. However, only neutron, proton, and $\alpha$-particle yields are significantly increased in this latter period and the neutron and proton yields are rather insensitive to the deformation. Thus only $\alpha$ particles show any sensitivity to the deformation in this latter period and here too the effect is not large.

The kinetic-energy spectra predicted from these simulations are indicated by the solid curves in Figs. 31 and 32. Overall these calculations give a better reproduction of the shape of the low-energy region for all detected charged particles and indicate that the sub-barrier enhancement is consistent with decay from highly deformed systems produced after most of the excitation energy is dissipated. The simulations do not reproduce the yield in the extreme subbarrier region for $^6$Li, $^7$Li, and $^7$Be fragments. However, sequential decay from B and other heavy unstable fragments, which were not included in the simulation, are expected to contribute here (e.g., Fig. 30). In any case one would not expect perfect agreement as the assumption of a single deformation is very simplistic. There should be either an equilibrium distribution of shapes for scenario (1) or for scenario (2) fluctuations in deformation are expected to develop in a time span of 5 zs [11]. Therefore the Coulomb-barrier distribution should be wider than that associated with a single deformation and the yields in the extreme sub-barrier region will be very sensitive to this width.

It has also been suggested that an increased yield of low-energy fragments can be caused by emissions from a compound system which has either expanded or its surface diffuseness has increased [2,5,35]. In fact the shape of the $\alpha$-particle, $^3$He, and $t$ spectra of this work can also be reproduced by including into the statistical model, transmission coefficients associated with a single reduced Coulomb barrier. Results which are almost identical in shape to the solid curves in Fig. 31 are obtained with spherical transmission coefficient, but where the radius parameters of the nuclear potentials are increased by a factor of 1.15. Similar spectra can also be obtained by increasing the diffuseness of the nuclear potential as well. To reproduce the experimental peak energy for Li and Be fragments, the radius parameters need to be scaled by larger factors. However even so, these calculations still do not reproduce the overall shape of the experimental spectra in the peak region. For example, the dotted curves in Fig. 32 were obtained with the radius parameters of the nuclear potentials increased by a factor of 1.25. The spectral peaks predicted in these calculations are all much narrower compared to the experimental data and somewhat narrower compared to the predictions for emission from a deformed system (solid curves). It is the distribution

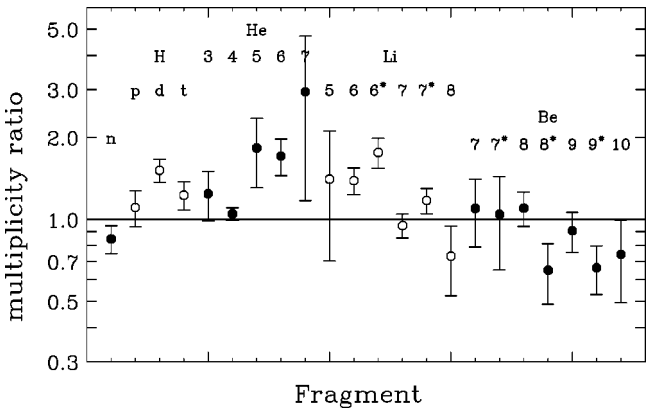


FIG. 33. Ratios of predicted to experimental multiplicities of the stable and unstable fragments from Table I. The predictions are statistical-model simulations from an initially deformed system (see the text).

of Coulomb barriers which is responsible for the broader peaks in the calculations for deformed systems and even wider distributions would be necessary to reproduce the width of the experimental spectra. Thus, although expansion and surface diffuseness effects can contribute to the experimental yield of low-energy Li and Be fragments, the full explanation requires a wide distribution of Coulomb barriers. Although we have stressed distributions of deformed compound nuclei as the source of this distribution, other mechanisms can contribute, for example, a monopole vibration.

The temperature-dependent level-density parameter used in all the calculations [Eq. (1)] was selected as it approximately reproduces the slopes of the high-energy tails of both the neutron and the $\alpha$-particle spectra. This was not possible with a temperature-independent parameter even for other estimates of the initial excitation energy. The simulations also give roughly the correct slope for the $^3$He spectrum (Fig. 31). However, for the other isotopes and for the $\alpha$ particles themselves, it should be recalled that the experimental spectra have nonstatistical components (Sec. III C and Ref. [9]). Irrespective of this uncertainty, these calculations demonstrate the advantage of measuring both neutron and charged particle spectra: $\alpha$ and the more exotic particles are emitted early in the decay and the temperature which characterizes the high-energy tails of the spectra are sensitive to the slope of the level density at the highest excitation energies. On the other hand, neutrons are emitted at all decay steps and the corresponding temperature is an average over all excitation energies. Better determination of the level-density parameter and its temperature dependence would require these spectra to be measured at larger angles, where the statistical contribution is expected to be dominant. Also a more accurate determination of the initial excitation energy would be helpful.

Figure 33 shows the ratios of the predicted (calculations with deformation) to the experimental multiplicities for the fragments listed in Table I. For hydrogen isotopes, the experimental multiplicities are from Gonin *et al.* [5] scaled by a factor of 2.3 (Sec. III C). Overall, the predictions are accurate to within a factor of 2. Again there is some uncertainty

TABLE II. Temperatures extracted from the ground- and excited-state populations of $^{6}$Li, $^{7}$Li, and $^{7}$Be fragments.

| Isotope | Temperature (MeV) |
|---|---|
| $^{6}$Li | $2.6\pm0.2$ |
| $^{7}$Li | $3.6\pm0.2$ |
| $^{7}$Be | $2.3\pm0.2$ |

in the experimental multiplicities due to the presence of nonstatistical components. Also uncertainties as to the exact values of the excitation energy and the level density affect these predictions. However, the results do indicate an enhanced emission of neutrons compared to these statistical model simulations, but considerably smaller than that obtained in Ref. [5]. At this stage it is difficult to make any firm statement as to whether the evaporation residues are more proton rich compared to their predicted location near the evaporation attractor line [14] until the composition of the nonstatistical emissions is known. In the nucleon-exchange transport code [27] these emissions are predominantly neutrons, which would then imply that the evaporation residues are somewhat more proton rich than we might expect.

### C. Temperature measurements

In a couple of the Monte Carlo simulations which were fit to experimental relative-energy distributions, a thermal distribution of excited states was assumed for a particular isotope, i.e., the probability for a level $i$ with spin $s_i$ and excitation energy $E_i^*$ is

$$P_i \propto (2s_i+1)\exp\left(\frac{E_i^*}{T}\right), \tag{2}$$

where $T$ is the temperature. As most of the exotic fragments are expected to be emitted early in the decay, the temperature is expected to be close to, but less than, the initial temperature of the compound nucleus. With an initial excitation energy of 240 MeV (Sec. IV A) and a level-density parameter between $A/8$ and $A/12$ MeV$^{-1}$, the initial temperature is 3.4–4.2 MeV. Therefore, the value of $T=3.7$ MeV used in the simulations is not unreasonable. Experimentally, information about this temperature can be determined from the multiplicities of $^{6,7}$Li and $^{7}$Be ground and excited states. In determining the temperature, sequential feeding from the first-excited particle-stable states of $^{7}$Li and $^{7}$Be to the ground states was considered. Also, for $^{6}$Li and $^{7}$Li, the ground-state yields were reduced by 13% due to feeding from B states (Sec. III D 1), but the error bars were increased by this amount. The temperatures from the three isotopes are listed in Table II. All are consistent with the assumed temperature, but the uncertainties are large. The weighted average is $3.4\pm0.9$ MeV. Note that a temperature extracted from $^{8}$Be yields has been omitted from the analysis due to the large expected feeding to the ground state from $^{9}$Be levels (Sec. IV A).

The uncertainty in the temperature therefore must be considered when evaluating the multiplicities of $^{10}$B, $^{11}$B, and $^{9}$Be states in Figs. 18 and 22. However, even if Eq. (2) describes the primary distribution, sequential feeding can modify it. Therefore a thermal distribution is only an approximation. The assumed temperature also affects the shape of the wide states ($^{5}$He, $^{5}$Li, $^{8}$Be*) used in the simulations [Eq. (A2)]. However, it will only make a significant modification to the intrinsic line shape if the temperature is less than or approximately equal to the natural width, which is not the case.

## V. CONCLUSION

Charged particles and neutrons detected in the angular range from 34° to 80° in coincidence with evaporation residues produced in the $E/A=11$ MeV $^{60}$Ni+$^{100}$Mo reaction have been studied. The measured neutron multiplicity is lower and the charged-particle multiplicities are larger than the corresponding values obtained by Gonin *et al.* [5] for the same reaction. The present results are more consistent with statistical-model calculations. The kinetic-energy spectra of charged particles are evaporationlike. However, their high-energy tails have angular distributions which indicate that there are nonstatistical components. Multiplicities of particle-unstable clusters emitted from the compound nucleus have been determined from the observed correlations in the emission of the light particles. The decays of the short-lived $^{5}$He and $^{8}$Be ($E^*=3.04$ MeV) states were found to be affected by the Coulomb field of the compound nucleus in accordance with theoretical estimates. The emission and sequential decay of the unstable clusters is shown to give rise to an enhancement of low-energy $\alpha$ particles as suggested in Ref. [9]. However, this enhancement is too small to account for the difference between the experimental spectrum and the predictions of standard statistical-model calculations. Only for the extreme low-energy portion of the spectrum, well below the peak, does this sequential component dominate the yield. The most important contributions are from $^{5}$He and $^{8}$Be ($E^*=3.04$ MeV) states. Sequential contributions are found to have similar affects on the $d$, $^{6,7}$Li, and $^{8}$Be spectra.

The origin of the sub-barrier enhancements is suggested to be a result of evaporation from highly deformed compound systems which are either produced dynamically during the fusion process or by thermal shape fluctuations. Statistical-model calculations incorporating a large initial deformation are shown to provide enhancements of approximately the right magnitude for all detected isotopes. However, as noted previously, a consistent description of sub-barrier enhancement could require additional mechanisms whose contributions may vary with excitation energy.

## ACKNOWLEDGMENTS

We would like to thank A. Galonsky for allowing us to borrow his neutron detectors. This work was supported by the Director, Office of High Energy and Nuclear Physics, Nuclear Physics Division of the U.S. Department of Energy under Contract Nos. DE-FG02-87ER-40316 and DE-FE05-86ER40256 and by The Robert A. Welch Foundation. Y.E.M. would like to thank Texas A&M University for its

hospitality and financial support during his two-month stay there.

## APPENDIX A: MONTE CARLO SIMULATIONS

The yield of particle-unstable fragments were determined by normalizing simulated relative-energy distributions of the decay products to the experimental data. These Monte Carlo simulations include the effects of the detector geometry, threshold, efficiency (neutrons), angular, and energy resolutions. The other important ingredients of these simulations are the initial distributions (angular and energy) of the primary fragment and the treatment of its decay.

The characteristics of the particle-unstable states (excitation energies, spins, decay widths, branching ratios) were taken from the compilations of Ajzenberg-Selove [36,37]. States with three-body exit channels are treated as two sequential two-body decays and all two-body decays are assumed to be isotropic. In a statistical model, the relative-energy distribution $F(\epsilon_{\rm rel})$ is determined from the intrinsic line shape $\rho_{\rm int}$ by

$$F(\epsilon_{\rm rel}) \propto \rho_{\rm int}(\epsilon_{\rm rel})\rho(E^* - \epsilon_{\rm rel}), \tag{A1}$$

where $\rho$ is the level density associated with all other degrees of freedom of the daughter nucleus and the emitted particle and $E^*$ is the total excitation energy. For large excitation energies this can be approximated as

$$F(\epsilon_{\rm rel}) \propto \rho_{\rm int}(\epsilon_{\rm rel})\exp\left(\frac{-\epsilon_{\rm rel}}{T}\right), \tag{A2}$$

where $T$ is the temperature. A temperature of 3.7 MeV was assumed in the simulations. However, the extracted fragment multiplicities are not very sensitive to the exact value of this temperature. For most states, a Lorentzian intrinsic line shape with FWHM set to the measured decay widths was assumed. However, Lorentzian shapes were not used for the broad $^5$He (g.s.), $^5$Li (g.s.), $^8$Be ($E^*=3.04$ MeV), and $^9$Be ($E^*=1.68$ MeV) states which are known to have asymmetric line shapes. The intrinsic line shape is related to the nuclear phase shift $\beta_{\rm N}$ by [38]

$$\rho_{\rm int}(\epsilon_{\rm rel}) = \frac{1}{\pi}\frac{d\beta_{\rm N}}{d\epsilon_{\rm rel}}. \tag{A3}$$

For these fragments, *R*-matrix fits [39–41] to experimental phase shifts were used to calculate the line shapes.

For states which decay to the short-lived $^5$He (g.s.) and $^8$Be ($E^*=3.04$ MeV) intermediates, the relative-energy distributions are determined in the same manner as in Refs. [23,42].

For all short-lived fragments ($\Gamma \gtrsim 100$ keV), the influence of the Coulomb field of the compound nucleus was considered. In the simulations, the trajectories of the primary fragments were followed for a time, the value of which is chosen from an exponential distribution appropriate for the measured decay width. Subsequently, the trajectories of the decay products in the Coulomb field were followed until their velocities approached their asymptotic values.

The primary energy spectrum of an unstable fragment is assumed to be identical to the measured ground-state spectrum, or where that is not available, the measured spectrum from neighboring stable isotopes was used. This assumption seem very reasonable as there are very few differences between the spectra for difference isotopes of the same element (Sec. III C) and in the case of the $^6$Li ($E^*=2.19$ MeV) fragment, the reconstructed primary energy spectra is identical, within the statistical errors, to the measured $^6$Li (g.s.) spectrum (Sec. III D 1). Thus, for example, the measured $^6$He (g.s.) spectrum was used when simulating the emission of $^5$He (g.s.), and the $^8$Be (g.s.) spectrum was used for the $^8$Be ($E^*=3.04$ MeV) simulation. These experimental spectra were fit to permit their extrapolation above and below the detector energy thresholds and to adjacent angular regions. The fits included contributions from two sources; an equilibrium (surface emission) source traveling with compound-nucleus velocity and a nonequilibrium (volume emission) source described by the parametrization of Ref. [43] with a source velocity of half the beam value. The Coulomb-barrier distributions for both sources were taken to be identical and Gaussian in shape. Due to the limited angular range of the experimental spectra, there is no unique set of multiplicities and temperatures associated with the two sources that can fit them. However, all parameter sets with produced good fits to the data produced similar extrapolations of these measured spectra above and below the detector thresholds. Therefore the choice of which parameter set to use is not important as long as the extracted statistical multiplicities are determined in the same manner as for the stable fragments (Sec. III C). For B and C primary fragments, their energy spectra was estimated using the fitted $^8$Be (g.s.) parameters, but with extrapolated Coulomb-barriers parameters.

## APPENDIX B: MULTIPLE HITS IN THE TELESCOPES

Events where two or more charged particles were incident on the same Si $E-\Delta E$ telescope were recorded in the experiment and identification of all the particles was often possible if each of these particles passed through a different strip of both the $E$ and $\Delta E$ detectors. Such events are important to include in the particle-particle correlation analysis. In fact for $^8$Be (g.s.), $^9$B (g.s.), and $^{12}$C ($E^*=7.65$ MeV) clusters, the sequential decay products have very small relative angles and the only time that these decay products are detected together is when they all are incident upon the same Si telescope. The difficulty in dealing with such events is that when more than two Si strips are hit in both the $E$ and $\Delta E$ detectors there is an ambiguity in determining which $E$ strip and which $\Delta E$ strip are associated with the same particle. This section describes the algorithm used to deal with this ambiguity.

The starting point for this algorithm is the $E-\Delta E$ maps generated from single-hit events, corrected for the nonuniformity of the $\Delta E$ detector. Tight contours are drawn around each of the prominent ''lines'' on these maps for particle identification. For double-hits events, there are two solutions to the ambiguity. For each solution there are two $E-\Delta E$ pairs giving a total of four possible pairs. Each pair is

checked to see if it lies within one of the contours associated with an identified particle. For 3% of the double-hit events, neither of the solutions have $E-\Delta E$ pairs both of which can be associated with identified particles and these events are discarded. For 57% of the events, only for one solution can both pairs be associated with identified particles and the ambiguity is considered broken. However, for the remaining 40% the ambiguity remains, i.e., all four $E-\Delta E$ pairs can be associated with identified particles. Of these events, 40% are discarded as both solutions contain at least one particle which punched through the Si $E$ detector and is unsuitable for the correlation analysis. This leave 24% of the events for which resolving the ambiguity is still a problem.

To further reduce the number of these events, one could consider drawing the particle identification contours more tightly around each of the lines on the $E-\Delta E$ maps. Rather than pursuing this course, a $\chi$-squared procedure was developed. A curve was drawn along the crest of each of the lines on the maps. The rms $\Delta E$ deviation of identified single-hit events from their respective curve was calculated and used to weight deviations from these curves. For the double-hit events, the weighted $\chi$-squared (sum of the weighted $\Delta E^2$ deviations for both $E-\Delta E$ pairs) was determined for each solution and the solution with the minimum $\chi$-squared was selected. To estimate the success of this method, single-hits events were combined to create pseudo-double-hit events. From these pseudoevents, it is estimated that of the remaining 24% of the real events, the ambiguity was correctly resolved 65% of the time. However, for 50% of the incorrectly resolved events, both particles are almost identical (same particle identification and same kinetic energy to within 1 MeV). The resolution of the ambiguity of these events is immaterial for constructing relative-energy distributions as whichever solution is chosen, the relative angle, and hence the relative energy, between the two fragments is identical. From this, the remaining number of badly identified events is estimated to be $\approx 4\%$. Note that a significant number of the real double-hit events are $\alpha-\alpha$ pairs from the decay of $^8$Be (g.s.) which are not found in the pseudoevents. Many of these $\alpha$ particles also have almost identical energies and so the ambiguity does not need to be resolved for these events as well. Triple-hit events were also analyzed with a similar algorithm.

## APPENDIX C: DETAILS OF GEMINI SIMULATIONS

The GEMINI statistical-model calculations of Sec. IV B are similar to that described in Ref. [9]. They include as evaporation channels, the ground and excited states of all H, He, Li, and Be isotopes. Excited states are limited to those with excitation energy less than 8 MeV and decay widths less than 2 MeV. Spherical transmission coefficients for the emission of clusters with $A>4$ were derived with nuclear potentials obtained from global optical-model fits to experimental $^6$Li, $^7$Li, and $^9$Be elastic-scattering data [44,45]. The use of transmission coefficients derived directly from the optical-model calculations may not be appropriate as there is significant absorption by the imaginary potential before the Coulomb barrier is reached. This absorption has been associated with the breakup of the cluster [46] and is thus inappropriate to include in transmission coefficients for the inverse evaporation process. The transmission coefficients used in the presented calculations were derived from the incoming-wave boundary-condition approximation [47] where all the absorption from the elastic channel occurs inside of the Coulomb barrier. The $^6$Li nuclear potential-energy function was used for the calculation of the transmission coefficients for all $A=5$ and 6, He and Li states (excited and ground state). Experimentally, $^6$Li optical-model potentials have been found to reproduce $^6$He elastic scattering data [48,49]. Similarly the $^7$Li nuclear potential energy was used for the heavier He and Li states. The $^9$Be nuclear potential was fitted with an $A$-dependent function in Ref. [45] which was used for all Be isotopes in this work. However, the $A$ dependence is not large.

For the emission of unstable fragments, the Hauser-Feshbach formalism should be extended by integrating over the intrinsic line shape. This is very time consuming for the wide states and so as an alternative the partial decay width for each unstable state was calculated at each step from a decay energy chosen in a Monte Carlo fashion from the appropriate intrinsic line shape. This procedure is expected to give correct results, on average, as long as the partial decay widths for these states are small compared to the total decay width. The intrinsic lines shapes used are the same as discussed in Appendix A.

[1] G. La Rana, D.J. Moses, W.E. Parker, M. Kaplan, D. Logan, R. Lacey, J.M. Alexander, and R.J. Welberry, Phys. Rev. C **35**, 373 (1987).

[2] R. Lacey, N.N. Ajitanand, J.M. Alexander, D.M. de Castro Rizzo, P. DeYoung, M. Kaplan, L. Kowalski, G. La Rana, D. Logan, D.J. Moses, W.E. Parker, G.F. Peaslee, and L.C. Vaz, Phys. Lett. B **191**, 253 (1987).

[3] G. La Rana, R. Moro, A. Brondi, P. Cuzzocrea, A. D'Onofrio, E. Perillo, M. Romano, F. Terrasi, E. Vardaci, and H. Dumont, Phys. Rev. C **37**, 1920 (1988).

[4] N.G. Nicolis, D.G. Sarantites, L.A. Adler, F.A. Dilmanian, K. Honkanen, Z. Majka, L.G. Sobotka, Z. Li, and T.M. Semkow, Phys. Rev. C **41**, 2118 (1990).

[5] M. Gonin, L. Cooke, K. Hagel, Y. Lou, J.B. Natowitz, R.P. Schmitt, S. Shlomo, B. Srivastava, W. Turmel, H. Utsunomiya, R. Wada, G. Nardelli, G. Nebbia, G. Viesti, R. Zanon, B. Fornal, G. Prete, K. Niita, S. Hannuschke, P. Gonthier, and B. Wilkins, Phys. Rev. C **42**, 2125 (1990).

[6] M. Kildir, G. La Rana, R. Moro, A. Brondi, A. D'Onofrio, E. Perillo, V. Roca, M. Romano, F. Terrasi, G. Nebbia, G. Viesti, and G. Prete, Phys. Rev. C **46**, 2264 (1992).

[7] J. Boger, J.M. Alexander, R.A. Lacey, and A. Narayanan, Phys. Rev. C **49**, 1587 (1994).

[8] B.J. Fineman, K.-T. Brinkmann, A.L. Caraley, N. Gan, R.L. McGrath, and J. Velkovska, Phys. Rev. C **50**, 1991 (1994).

[9] R.J. Charity, M. Korolija, D.G. Sarantites, and L.G. Sobotka, Phys. Rev. C **56**, 873 (1997).
[10] J.F. Liang, J.D. Bierman, M.P. Kelly, A.A. Sonzogni, R. Vandenbosch, and J.P.S. van Schagan, Phys. Rev. C **56**, 908 (1997).
[11] R.J. Charity, Phys. Rev. C **61**, 054614 (2000).
[12] B.S. Pudliner, V.R. Pandharipande, J. Carlson, and R.B. Wiringa, Phys. Rev. Lett. **74**, 4396 (1995).
[13] M. Gonin, L. Cooke, K. Hagel, Y. Lou, J.B. Natowitz, R.P. Schmitt, B. Srivastava, W. Turmel, H. Utsunomiya, R. Wada, B. Fornal, G. Nardelli, G. Nebbia, G. Viesti, R. Zanon, G. Prete, P. Gonthier, and B. Wilkins, Phys. Lett. B **217**, 406 (1989).
[14] R.J. Charity, Phys. Rev. C **58**, 1073 (1998).
[15] I. Tilquin, Y. El Masri, M. Parlog, Ph. Collon, M. Hadri, Th. Keutgen, J. Lehmann, P. Leleux, P. Lipnik, A. Ninane, F. Hanappe, G. Bizard, D. Durand, P. Mosrin, J. Péter, R. Régimbart, and B. Tamain, Nucl. Instrum. Methods Phys. Res. A **365**, 446 (1995).
[16] C. Wagemans, *The Nuclear Fission Process* (CRC Press, Boca Raton, FL, 1991), Chap. 11.
[17] J.K. Dickens, computer code SCINFUL, ORNL-6462, 1988, NEA Data Bank Program: PSR-0267, 1994.
[18] D.G. Foster, Jr. and D.W. Glasgow, Phys. Rev. C **3**, 576 (1971).
[19] R.J. Charity, J.F. Dempsey, and L.G. Sobotka (unpublished).
[20] J. F. Ziegler, computer code TRIM, 1995 version, www.research.ibm.com/ionbeams/home.htm
[21] R.J. Charity, M.A. McMahan, G.J. Wozniak, R.J. McDonald, L.G. Moretto, D.G. Sarantites, L.G. Sobotka, G. Guarino, A. Pantaleo, L. Fiore, A. Gobbi, and K.D. Hildenbrand, Nucl. Phys. **A483**, 371 (1988).
[22] R.J. Charity, K.X. Jing, D.R. Bowman, M.A. McMahan, G.J. Wozniak, L.G. Moretto, N. Colonna, G. Guarino, A. Pantaleo, L. Fiore, A. Gobbi, and K.D. Hildenbrand, Nucl. Phys. **A511**, 59 (1990).
[23] J. Pochodzalla, C.K. Gelbke, W.G. Lynch, M. Maier, D. Ardouin, H. Delagrange, H. Doubre, C. Grégoire, A. Kyanowski, W. Mittig, A. Péghaire, J. Péter, F. Saint-Laurent, B. Zwieglinski, G. Bizard, F. Lefèbvres, B. Tamain, J. Québert, Y.P. Viyogi, W.A. Freidman, and D.H. Boal, Phys. Rev. C **35**, 1695 (1987).
[24] R.J. Charity, J. Barreto, L.G. Sobotka, D.G. Sarantites, D.W. Stracener, A. Chbihi, N.G. Nicolis, R. Auble, C. Backtash, J.R. Beene, F. Bertrand, M. Halbert, D.C. Hensley, D.J. Horen, C. Ludemann, M. Thoennessen, and R. Varner, Phys. Rev. C **46**, 1951 (1992).
[25] R.J. Charity, computer code GEMINI (unpublished), URL http://www.chemistry.wustl.edu/~rc
[26] A.J. Sierk, Phys. Rev. C **33**, 2039 (1986).
[27] S.J. Luke, R. Vandenbosch, and J. Randrup, Phys. Rev. C **48**, 857 (1993).
[28] E. Holub, D. Hilscher, G. Ingold, U. Jahnke, H. Orf, and H. Rossner, Phys. Rev. C **28**, 252 (1983).
[29] E. Holub, D. Hilscher, G. Ingold, U. Jahnke, H. Orf, H. Rossner, W.P. Zank, W.U. Schröder, H. Gemmeke, K. Keller, L. Lassen, and W. Lücking, Phys. Rev. C **33**, 143 (1986).
[30] H. Feldmeier, computer code HICOL [Prog. Phys. **50**, 915 (1987)].
[31] M. Cinausero, G. Prete, D. Fabris, G. Nebbia, G. Viesti, G.X. Dai, K. Hagel, J. Li, Y. Lou, J.B. Natowitz, D. Utley, R. Wada, N. Gelli, F. Lucarelli, and M. Colanna, Phys. Lett. B **383**, 372 (1996).
[32] M. Thoennessen, J.R. Beene, F.E. Bertrand, C. Baktash, M.L. Halbert, D.J. Horen, D.G. Sarantites, W. Spang, and D.W. Stracener, Phys. Rev. Lett. **70**, 4055 (1993).
[33] R.G. Stokstad and E.E. Gross, Phys. Rev. C **23**, 281 (1981).
[34] J.R. Huizenga, A.N. Behkami, I.M. Govil, W.U. Schröder, and J. Tõke, Phys. Rev. C **40**, 668 (1989).
[35] X.S. Chen, C. Ngô, E. Tomasi, M. Barranco, X. Viñas, and H. Ngô, Nucl. Phys. **A401**, 143 (1983).
[36] F. Ajzenberg-Selove, Nucl. Phys. **A490**, 1 (1988).
[37] F. Ajzenberg-Selove, Nucl. Phys. **A506**, 1 (1990).
[38] G.C. Phillips, T.A. Griffy, and L.C. Biedenharn, Nucl. Phys. **21**, 327 (1960).
[39] Th. Stammbach and R.L. Walters, Nucl. Phys. **A180**, 225 (1972).
[40] C.M. Jones, G.C. Phillips, and P.D. Miller, Phys. Rev. **117**, 525 (1960).
[41] F.C. Barker, Can. J. Phys. **61**, 1371 (1983).
[42] R.J. Charity, L.G. Sobotka, N.J. Robertson, D.G. Sarantites, J. Dinius, C.K. Gelbke, T. Glasmacher, D.O. Handzy, W.C. Hsi, M.J. Huang, W.G. Lynch, C.P. Montoya, G.F. Peaslee, C. Schwarz, and M.B. Tsang, Phys. Rev. C **52**, 3126 (1995).
[43] T.C. Awes, G. Poggi, C.K. Gelbke, B.B. Back, B.G. Glagola, H. Breuer, and V.E. Viola, Jr., Phys. Rev. C **24**, 89 (1981).
[44] J. Cook, Nucl. Phys. **A388**, 153 (1982).
[45] R. Balzer, M. Hugi, B. Kamys, J. Lang, R. Müller, E. Ungricht, J. Unternährer, L. Jarczyk, and A. Strzałkowski, Nucl. Phys. **A293**, 518 (1977).
[46] G.R. Satchler, *Introduction to Nuclear Reactions*, 2nd ed. (Oxford University Press, New York, 1990), p. 197.
[47] J.M. Alexander, M.T. Magda, and S. Landowne, Phys. Rev. C **42**, 1092 (1990).
[48] R.J. Smith, J.J. Kolata, K. Lamkin, A. Morsad, K. Ashtorab, F.D. Becchetti, J.A. Brown, J.W. Janecke, W.Z. Liu, and D.A. Roberts, Phys. Rev. C **43**, 761 (1991).
[49] R.E. Warner, F.D. Becchetti, J.W. Jänecke, D.A. Roberts, D. Butts, C.L. Carpenter, J.M. Fetter, A. Muthukishnan, J.J. Kolata, K. Lamkin, M. Belbot, M. Zahar, A. Golonsky, K. Ieki, and P. Zecher, Phys. Rev. C **51**, 178 (1995).